The Pennsylvania State University

The Graduate School

FUNDAMENTAL UNDERSTANDING INTO BIMODAL POWDER SIZE DISTRIBUTIONS IN BINDER JETTING ADDITIVE MANUFACTURING PROCESS

A Thesis in

Additive Manufacturing and Design

by

Ana Paula Clares Pastrana

Submitted in Partial Fulfillment
of the Requirements
for the Degree of

Master of Science

May 2022

The thesis of Ana Paula Clares Pastrana was reviewed and approved by the following:

Guha Manogharan
Assistant Professor of Mechanical Engineering
Thesis Advisor

Timothy Simpson
Interim Department Head,
School of Engineering Design, Technology, and Professional Programs
Paul Morrow Professor in Engineering Design and Manufacturing

Edward Reutzel
Director, CIMP-3D
Associate Research Professor

Allison Beese
Director of Additive Manufacturing and Design Graduate Program
Associate Professor

ABSTRACT

Additive Manufacturing (AM) is a novel, disruptive technology that fabricates objects layer by layer from three-dimensional (3D) data. Binder jetting is a powder bed-based AM technology that selectively deposits liquid binder droplets to join powder particles. These steps are repeated layer by layer until the entire part is fabricated. Upon fabrication, the binder is cured, and additional post-processing steps are required to achieve final part microstructure and properties. The process offers unique advantages when compared to other AM technologies, including high production rates, absence of heat-induced defects during printing, large build volumes, part nesting, powder recycling, and no need for support structures. Additionally, a wide variety of materials can be used, such as metals, ceramics, and sand. However, one of the biggest challenges still present in binder jetting is achieving fully dense parts, making the as-printed products unsuitable for most structural applications.

Although there are many known parameters that affect the part's quality in binder jetting, particle size distribution has been demonstrated to have a significant impact on green and sintered density. Bimodal size distributions offer an alternative to improve the printed part's density and mechanical performance. The increase in density from the bimodal particle mixture can be attributed to its ability to pack more tightly, as finer particles will fill the void spaces created between the coarser powder. Despite the available literature investigating bimodal size mixtures, findings are material-dependent or only evaluated on certain properties. This thesis provides an investigation relying on novel computational models coupled with experimental efforts to understand the fundamental impact bimodal mixtures have on packing density, sintered density, and mechanical properties utilizing two different materials.

The role different particle size distributions have on packing density, flowability, and porosity was investigated through computational approaches. Computational simulations of

powder spreading were developed based on the discrete-element-method (DEM), where three different ceramic particle size groups were carefully selected for their quantitative evaluation and comparison. Results illustrate an improvement in packing density with the introduction of bimodal size distributions. These results were experimentally validated with 316L stainless steel using an Innovent+ binder jetting machine. The investigation was conducted using AM fabricated cylinders and bar coupons; these coupons were printed using six different particle size groups and their sintered density and mechanical performance was assessed. Techniques such as X-ray computed tomography (XrCT), geometry measurements, and three-point bending tests were employed as tools to collect density and ultimate flexural strength (UFS) data from each group. Statistical comparisons from UFS and sintered density data demonstrate that the use of bimodal size groups improves part performance.

Overall, this thesis highlights the important role particle size distribution plays during the binder jetting process. Outcomes of this study serve to accelerate the inclusion of bimodal size distributions in industry and academia to help overcome current limitations in achieving high-density parts.

TABLE OF CONTENTS

LIST OF FIGURES

LIST OF TABLES

ABREVIATIONS AND NOMENCLATURE

AM	Additive Manufacturing
ASTM	American Society of Testing and Materials
XrCT	X-ray Computed Tomography
DfAM	Design for Additive Manufacturing
DED	Directed Energy Deposition
LPBF	Laser Powder Bed Fusion
CAD	Computer-Aided Design
DEM	Discrete-Element-Method
XrCT	X-ray Computed Tomography
UFS	Ultimate Flexural Strength
a	Acceleration (m/s)
D	Roller Diameter (cm)
d	Diameter (μm)
f	Packing Fraction Adjustment
F	Total Force Between Particles (N)
F_c	Contact Force (N)
F_e	Elastic Force (N)
F_n	Force in Normal Direction (N)
F_t	Force in Tangential Direction (N)
H	Roller Height (cm)
k	Spring Constant
K	Bonding Number
m	Mass of Particle (g)

P	Particles Required
r	Radius (cm)
u	Relative Velocity (m/s)
v	Particle Velocity (m/s)
V_d	Domain Volume (cm^3)
V_{total}	Total Cavities Present (cm^3)
V_{wp}	Wall-Particle Cavity Volume (cm^3)
x	Particle
γ	Surface Energy (N/m)
δ	Displacement (cm)
η	Damping Coefficient
g	Gravity (cm/s^2)
y	Moving Distance (cm)
ρ	Density (g/cm^3)
$m_{cylinder}$	Cylinder mass (g)
$v_{cylinder}$	Cylinder volume (cm^3)
F	Force to rupture (N)
L	Distance between center of supporting rods (cm)
w	Specimen width (cm)
t	Specimen thickness (cm)

ACKNOWLEDGEMENTS

First, I would like to thank my family for the unconditional love and support they have provided me throughout this whole process. For giving me the opportunities they have, and for the non-stop encouragement when I needed it the most.

I would like to thank my advisor Dr. Guha Manogharan, for seeing potential in me and letting me join the Systems for Hybrid-Additive Process Engineering (SHAPE) Lab as I started my path in the additive manufacturing industry. I will always be grateful for his mentorship, for the countless learning opportunities he provided me, for his advice and feedback, for trusting me, and for always being there for me.

I would like to thank Dr. Simpson, Dr. Beese, and Jaclyn Stimely for all the hard work they have put into making the Additive Manufacturing and Design program at Penn State a competitive, comprehensive, and outstanding program that has given me the chance of becoming a knowledgeable person in the additive manufacturing industry with a lot of opportunities.

I am grateful to Dr. Reutzel for sharing his knowledge and insight in the classroom and for his feedback in preparation for this thesis. I am thankful to all my professors and lab mates for all their advice and contribution to my work. I would like to thank Tim Stecko, EOS, ExOne, and FLOW 3D for their support, help, and for the valuable learning experiences.

Finally, I am very grateful for all the amazing people I met during my time at Penn State. To my best friends, Lauren Katch and Ryan Stebbins, and to all my other friends, thank you for all the support, help, motivation, fun times, and very valuable memories we lived together.

This work was funded by NSF CAREER CMMI #1944120 and the support from 2020 PA Manufacturing Fellows Initiative Grant. The findings and conclusions do not necessarily reflect the view of the funding agency.

Chapter 1

Introduction

This chapter covers the background, relevant literature review, motivations, objectives, and the overall organization of the thesis.

Additive manufacturing (AM) is a disruptive technology that is highly renowned all over the world. The American Society for Testing and Materials (ASTM) describes AM as the process of joining materials layer by layer to make objects from three-dimensional (3D) data [1]. AM differs from traditional subtractive methods as they use material removal techniques such as milling, machining, carving, and shaping [2]. The advancement of AM technology was made possible due to a digital transformation, which allowed engineers to translate ideas and thoughts into models using computer-aided designs (CAD). This novel process is also known as additive fabrication, rapid prototyping, layer manufacturing, freeform fabrication, or 3D printing.

Additive manufacturing traces its origins back to the 1980s when the first pioneering company, 3D Systems [3], developed an AM technology currently known as stereolithography (SLA). This process uses ultraviolet (UV) light-sensitive liquid photopolymers to fabricate parts. Since the first appearance of SLA, additive manufacturing quickly gained momentum from the U.S. to England, Japan, Germany, Israel, China, the Netherlands, and the rest of the world. In the past couple of decades, the number of scientific publications and patents referring to additive manufacturing has significantly increased [4], [5]. According to Global Market Trajectory & Analytics, it was estimated that the global AM and Materials market in 2020 was US$15.4 billion and expected to expand to US$62.2 billion by 2027 [6]. This promising economic growth has put AM technology in high demand in industries such as automotive, energy, health, dental, food, space, foundry, and aerospace [5], [7], [8].

Currently, there are seven different techniques within the umbrella of additive manufacturing. Each technique can be distinguished by employing different types of equipment and involving different physical phenomena to fabricate desired geometry. Additionally, one of the main differences among the AM processes lies in the type of feedstock used: solid, liquid, or powder [5]. Techniques that employ solid based feedstock include, sheet lamination, directed energy deposition (DED), and material extrusion (often referred to as fused deposition modeling or fused filament fabrication [9], [10]). Liquid based technologies include vat photopolymerization (often referred to as stereolithography (SLA) or digital light processing (DLP)), and material jetting (often referred to as PolyJet, and Multi Jet Modeling). Powder feedstock can be found in powder bed fusion (PBF), (often referred to as selective laser sintering (SLS) and direct metal laser sintering (DMLS)), directed energy deposition (DED), and binder jetting. More detailed information about the specific AM processes mentioned can be found in [1].

The three different powder bed-based technologies bring different benefits and limitations with them. PBF uses thermal energy from either a laser or electron beam to selectively fuse regions of a powder together [1]. The PBF process can be used for polymers and metallic materials, providing fully dense, complex, and dimensionally accurate parts [11]. DED also relies on thermal energy from either a laser, electron beam, or arc, producing layers of material by melting the feedstock as it flows into the focal point of the energy source [1]. The DED process works with ceramics and metals, allowing for fully dense parts, high single-point deposition rates, and functionally graded components with composition variations in the X, Y, and Z directions [12]. Finally, the last type of AM process in this category is binder jetting, the focus of this thesis.

Binder jetting was developed in 1993 by the Massachusetts Institute of Technology (MIT) [13]. The process involves the selective deposition of a liquid bonding agent in the form of droplets, which are typically 80 μm in size, to join powder particles together [1]. The AM fabrication begins by spreading a thin layer of powder into the build box assisted by a blade, rake, or rotating roller.

Then, a printhead containing an array of nozzles selectively jets a binder solution onto the powder, following the desired geometry. Upon completion of droplet deposition, a heat lamp goes over the powder bed surface to partially cure the binder. After this, the build platform is lowered, and a new layer of powder is spread. These steps are repeated layer by layer until final fabrication is achieved. When the printing process is completed, the build box is removed from the machine and placed in an oven to cure the binder solution. At this stage, the geometry is known as a "green part", displaying relatively low strength and requires manual or compressed air de-powdering. Depending on the desired outcome, these parts require post-processing steps to burn out the binder, densify the part, and bring the final geometry to specification. Such steps are sintering, material infiltration, polishing, and finishing [14].

Binder jetting can be configured to offer multiple unique advantages when compared to other AM technologies. Such benefits include full-color printing, high production rates, low costs, no need for support structures, repeatability and accuracy, large build volumes, part nesting, powder recycling, and high-speed production [14], [15]. Additionally, since no high energy sources are used during printing, heat-induced defects common in PBF and DED, like part distortion and warping, are not present. This allows for a large selection of materials such as metals, ceramics, and sands [14], [16].

Metals are one of the most popular types of materials used with binder jetting technology; their application in the industry has been rapidly growing, shown by the emergence of new projects and the development of new production machines [8], [15]. The absence of residual stresses in this process has shown to be very promising for additively manufacturing complex metal alloys that are difficult to manufacture traditionally, such as Inconel and cobalt-chrome alloys [8]. Other metallic materials that are currently used in the binder jetting process by academia and industry are ferrous alloys (stainless steels), nickel alloys, titanium alloys, and copper, among others [15]. Binder jetting has also gained popularity as an alternative method for the fabrication of ceramics because they are

even more difficult to cast and machine than most complex metal alloys [17]. Ceramics are notorious for having issues with thermal gradients and internal stresses that may initiate cracks and cause the brittle material to break. Binder jetting is an ideal candidate for ceramics due to its ability to build at low temperatures. Popular engineering ceramic materials used in binder jetting include alumina, silicon carbide, silicon nitride, zirconia, and many others [18].

Although there are clear advantages offered by binder jetting, there are drawbacks that must be addressed. One of the main limitations is the relatively low densities that can be achieved from the fabricated parts. The weak and brittle green state parts [14], [17] offer significant porosity and poor mechanical properties. This is due to the lack of fully fusion since the material is only joined by the cured binder. These weaker intermediary shapes need extensive post-processing. For fully dense and reliable parts, additional steps are required, which add time, steps, costs, and possible defects such as part shrinkage. Another limitation of this process is the lack of predictive models available for binder-powder interactions and printed quality [15], [19]. Without predictive models, there is an unknown factor to the spreadability of novel powder materials and particle sizes, as well as the surface interaction with binder solution. This lack of knowledge adds uncertainties regarding the accuracy and strength of the fabricated parts [20].

Like other AM processes, in binder jetting, multiple factors influence the final quality and structural integrity of the desired part. The main factors affecting green part fabrication quality are process-related and material-related parameters [15], [19], [21]. Process-related includes any machine parameters that are directly referenced by the hardware/software during the printing process. Some of the most impactful include: (1) layer thickness, which controls the amount of powder that is spread on each layer, (2) spreading speed, which is the rate at which powder is spread during each layer, and (3) binder saturation, which is the amount of binder solution used during printing (ratio of binder volume to open pore volume in the powder bed). Although many other parameters exist, an appropriate selection of the above mentioned is essential to control the

uniformity of spreading, mechanical strength properties, dimensional accuracy, structural integrity, resolution, and surface roughness [8], [14], [19], [22]– [24]. Efforts for optimization have been considered in the literature showing the importance of an adequate selection [23], [24].

Material-related parameters include physical and chemical properties regarding the feedstock and binder system. These parameters can be the binding agents, and the properties of feedstock. Binding agents include the binder materials that should be appropriately selected as they directly affect wettability and permeation on the powder, based on the saturation used. Properties of feedstock, refer to the powder characteristics, both bulk and specific [15]. Specific powder characteristics refer to the particle size distribution and morphology (shape of the powder). Bulk characteristics of the feedstock are generalized as the aggregate behavior of all particles and can be measured through packing, flowability, and spreadability. An appropriate selection can enhance powder bed conditions, leading to increased green density, porosity reduction, and shrinkage mitigation.

This thesis focuses on particle size distribution as it has been found to significantly impact the green and sintered strength, packing density, and flowability of binder jetting parts [25]. Finer particle sizes have been linked to higher packing densities and improved sinterability due to the large surface energy that results in a higher particle bonding rate [15]. However, fine particles have shown a detrimental impact on flowability due to agglomeration and high interparticle cohesiveness compared to coarser ones [21]. Spherical morphology, bimodal particle size distributions (consisting of a combination of fine and coarse particles), have been used in literature to overcome binder jetting's low apparent densities [17]. The combination of both particle sizes is used to fill more void spaces created as the particles pack. This thesis' motivation and central hypothesis are that bimodal powder size distributions can be utilized in binder jetting to increase density and result in higher mechanical performance, regardless of the material used. In our work, two different materials were selected to prove this concept.

Chapter 2 focuses on simulating the powder spreading stage in binder jetting using ceramic material. FLOW-3D AM v5 CFD software (release 3, Flow Science) was used to perform the simulations relying on the discrete-element-method (DEM). Three simulations were generated corresponding to two unimodal and one bimodal size distribution, and the setup parameters were carefully chosen for each different group. The main objective of this portion of the thesis is to quantify the impact different particle size distributions have on flowability, density, and porosity. Chapter 3 focuses on the binder jetting fabrication using 316L stainless steel material. This portion details the experimental work performed using six particle size groups containing unimodal and bimodal distributions. Caliper measurements, X-ray computed tomography (XrCT) and three-point bending are used for comparison. The main objective of this portion of the thesis is to validate the computational work proving the advantage of bimodal mixtures and evaluate their impact on sintered density and mechanical performance. Chapter 4 summarizes the work in this thesis, presenting the major findings obtained, limitations, and future work.

References

[1] "Designation: F2792 − 12a," doi: 10.1520/F2792-12A.

[2] "What is Additive Manufacturing | GE Additive." https://www.ge.com/additive/additive-manufacturing (accessed Feb. 27, 2022).

[3] "3D Printers, Software, Manufacturing & Digital Healthcare | 3D Systems." https://www.3dsystems.com/ (accessed Feb. 27, 2022).

[4] M. Upadhyay, T. Sivarupan, and M. El Mansori, "3D printing for rapid sand casting—A review," Journal of Manufacturing Processes, vol. 29. Elsevier Ltd, pp. 211–220, Oct. 01, 2017, doi: 10.1016/j.jmapro.2017.07.017.

[5] O. Abdulhameed, A. Al-Ahmari, W. Ameen, and S. H. Mian, “Additive manufacturing: Challenges, trends, and applications:,” https://doi.org/10.1177/1687814018822880, vol. 11, no. 2, pp. 1–27, Feb. 2019, doi: 10.1177/1687814018822880.

[6] “Additive Manufacturing & Material - Global Market Trajectory & Analytics.” https://www.researchandmarkets.com/reports/4804521/additive-manufacturing-and-material-global (accessed Feb. 27, 2022).

[7] T. Wohlers and T. Gornet, “History of Additive Manufacturing,” 2014.

[8] M. Ziaee and N. B. Crane, “Binder jetting: A review of process, materials, and methods,” Addit. Manuf., vol. 28, pp. 781–801, Aug. 2019, doi: 10.1016/J.ADDMA.2019.05.031.

[9] D. J. Braconnier, R. E. Jensen, and A. M. Peterson, “Processing parameter correlations in material extrusion additive manufacturing,” Addit. Manuf., vol. 31, p. 100924, Jan. 2020, doi: 10.1016/J.ADDMA.2019.100924.

[10] S. I. Park, D. W. Rosen, S. kyum Choi, and C. E. Duty, “Effective mechanical properties of lattice material fabricated by material extrusion additive manufacturing,” Addit. Manuf., vol. 1–4, pp. 12–23, Oct. 2014, doi: 10.1016/J.ADDMA.2014.07.002.

[11] D. Dev Singh, T. Mahender, and A. Raji Reddy, “Powder bed fusion process: A brief review,” Mater. Today Proc., vol. 46, pp. 350–355, Jan. 2021, doi: 10.1016/J.MATPR.2020.08.415.

[12] I. Gibson, D. Rosen, and B. Stucker, “Directed Energy Deposition Processes,” Addit. Manuf. Technol., pp. 245–268, 2015, doi: 10.1007/978-1-4939-2113-3_10.

[13] “US5204055A - Three-dimensional printing techniques - Google Patents.” https://patents.google.com/patent/US5204055A/en (accessed Nov. 17, 2020).

[14] I. Gibson, D. Rosen, B. Stucker, and M. Khorasani, “Binder Jetting,” Addit. Manuf. Technol., pp. 237–252, 2021, doi: 10.1007/978-3-030-56127-7_8.

[15] M. Li, W. Du, A. Elwany, Z. Pei, and C. Ma, “Metal binder jetting additive manufacturing: A literature review,” J. Manuf. Sci. Eng. Trans. ASME, vol. 142, no. 9, Sep. 2020, doi: 10.1115/1.4047430/1084395.

[16] Y. Bai and C. B. Williams, “An exploration of binder jetting of copper,” Rapid Prototyp. J., vol. 21, no. 2, pp. 177–185, Mar. 2015, doi: 10.1108/RPJ-12-2014-0180/FULL/PDF.

[17] W. Du, X. Ren, Z. Pei, and C. Ma, “Ceramic Binder Jetting Additive Manufacturing: A Literature Review on Density,” J. Manuf. Sci. Eng., vol. 142, no. 4, Apr. 2020, doi: 10.1115/1.4046248.

[18] B. Mansfield, S. Torres, T. Yu, and D. Wu, “A Review on Additive Manufacturing of Ceramics,” ASME 2019 14th Int. Manuf. Sci. Eng. Conf. MSEC 2019, vol. 1, Nov. 2019, doi: 10.1115/MSEC2019-2886.

[19] H. Miyanaji, “Binder jetting additive manufacturing process fundamentals and the resultant influences on part quality.,” 2018, doi: 10.18297/etd/3058.

[20] I. Gibson, D. Rosen, and B. Stucker, “Additive manufacturing technologies: 3D printing, rapid prototyping, and direct digital manufacturing, second edition,” Addit. Manuf. Technol. 3D Printing, Rapid Prototyping, Direct Digit. Manuf. Second Ed., pp. 1–498, Jan. 2015, doi: 10.1007/978-1-4939-2113-3.

[21] S. Mirzababaei and S. Pasebani, “A Review on Binder Jet Additive Manufacturing of 316L Stainless Steel,” J. Manuf. Mater. Process. 2019, Vol. 3, Page 82, vol. 3, no. 3, p. 82, Sep. 2019, doi: 10.3390/JMMP3030082.

[22] N. Lecis et al., “Effects of process parameters, debinding and sintering on the microstructure of 316L stainless steel produced by binder jetting,” Mater. Sci. Eng. A, vol. 828, p. 142108, Nov. 2021, doi: 10.1016/J.MSEA.2021.142108.

[23] S. Shrestha and G. Manogharan, “Optimization of Binder Jetting Using Taguchi Method,” vol. 69, doi: 10.1007/s11837-016-2231-4.

[24] H. Chen and Y. F. Zhao, “Process parameters optimization for improving surface quality and manufacturing accuracy of binder jetting additive manufacturing process,” Rapid Prototyp. J., vol. 22, no. 3, pp. 527–538, 2016, doi: 10.1108/RPJ-11-2014-0149/FULL/PDF.

[25] W. Du, J. Roa, J. Hong, Y. Liu, Z. Pei, and C. Ma, “Binder Jetting Additive Manufacturing: Effect of Particle Size Distribution on Density,” J. Manuf. Sci. Eng. Trans. ASME, vol. 143, no. 9, Sep. 2021, doi: 10.1115/1.4050306/1100582.

Chapter 2

Discrete–Element Simulation of Powder Spreading Process in Binder Jetting, and the Effects of Powder Size

This Chapter has been accepted for publication at the Proceedings of the ASME 2021 16th International Manufacturing Science and Engineering Conference (MSEC2021). (https://doi.org/10.1115/MSEC2021-63351): A. Paula Clares and G. Manogharan, "Discrete-Element Simulation of Powder Spreading Process in Binder Jetting, and the Effects of Powder Size," 2021, Accessed: Jan. 23, 2022. [Online].

Abstract

Binder jetting has gained particular interest amongst additive manufacturing (AM) techniques because of its wide range of applications, broader feasible material systems, and absence of rapid melting-solidification issues present in other AM processes. Understanding and optimizing printing parameters during the powder spreading process is essential to improve the quality of the final part. In this study, a discrete-element-method (DEM) simulation is employed to evaluate the powder packing density, flowability, and porosity during powder spreading process utilizing three different powder groups. Two groups are formed with unimodal size distributions (75-84 μm and 100-109 μm), and the third one consisting of a bimodal distribution (50 μm +100 μm).

A thorough investigation into the effects of powder size distribution during the powder spreading step in a binder jetting process is conducted using ceramic foundry sand. It was observed that coarser particles result in higher flowability (62% decrease in repose angle) than finer ones due to the cohesion effect present in the latter. A bimodal size distribution yields the highest packing density (8% increase) and lowest porosity (~12% reduction) in the powder bed, as the finer particles fill in the voids created between the coarser ones. Findings from this study are directly applicable to binder jetting AM process and offer new insights for AM powder manufacturers.

Keywords: additive manufacturing, ceramics, binder jetting, powder size, porosity, layer density, flowability.

2.1 Introduction

Additive manufacturing (AM) has gained significant popularity due its ever-growing capabilities to join materials layer by layer based on three-dimensional (3D) model data [1], offering a wide array of applications [2], [3]. Among the several recent advancements in AM, powder bed-based processes have garnered significant attention due to their finer resolution, higher part quality, powder reusability [4], and functional parts [5]. This study focuses on binder jetting, a process in which a liquid binding agent is selectively deposited to join powder materials [6].

Among the seven AM processing categories [7], binder jetting has gained a spotlight of its own, as the process is one of the most promising techniques to work with ceramic materials [6]. Because of their physical properties, ceramics cannot be easily casted or machined and hence, AM offers a viable technology for production of ceramic parts with higher geometrical complexity [8]. Ceramics offer unique characteristics, such as biocompatibility, hardness, and resistance to wear, heat, and corrosion [9], which are ideal for aerospace [10], [11], biomedical[12]–[14], and other applications[15], [16]. Although ceramic binder jetting is a relatively simpler AM process which does not require expensive lasers or electron beams, additional steps for post-printing such as de-powdering, curing, de-binding, and sintering are necessary to achieve a fully dense part.

Since binder jetting is a powder bed-based technology, it is essential to understand the underlying physics of powder particle interaction during the spreading process which has a significant impact on the characteristics and quality of the final product [17], [18]. Binder jetting employs a relatively larger powder size distribution (when compared with other AM technologies [19], [20]) which requires post-processing to achieve non-porous fully dense parts [21]. Bai et al.

[21] demonstrated an improvement in powder packing density and flowability (10.5% increase) through the use of bimodal powder size distribution in copper powders. Chen et al. [22] evaluated a counter-rolling powder spreading process and the effects of spreading speed. It was found that a higher spreading speed reduced the packing density as drag forces on particles from the roller become stronger, reducing the mass flow rate. However, this phenomenon is further amplified in bimodal particle size distribution which is investigated in this paper for better understanding.

Because of the significant time and cost implications of full factorial experimental investigations of the powder spreading process in AM, numerical simulations such as the discrete-element-method (DEM) have manifested as an effective way to simulate the spreading process at a particle scale [6], [23]–[26]. Many investigations based on DEM have focused on predicting layer density and resulting mechanical strength using spherical particles [26], [27]. Miao et al. [6] employed the DEM in ceramic binder jetting to simulate the powder spreading process in order to study the influence of layer thickness and roller diameter on powder bed density. This study highlighted the need to further research the effects of particle size distribution in binder jetting. Similarly, Lee et al. [28] developed a DEM model to understand the powder packing dynamics in AM with varying size distributions. This study noted that a mix of powder diameters results in an improvement of packing density.

Du et. al [29] employed analytical modeling and experimental methods to optimize powder ratios for the highest tap density in a silicon carbide ceramic part. The results highlighted the use of a modeling method to predict the tap density of bimodal powders with high accuracy. Similar outcomes were found by Bai et. al [30], where bimodal mixtures led to improved apparent and tap densities across several material systems. The study characterized improvements in powder bed density and sintered density with the introduction of the bimodal distributions. Other works, however, such as in [31], found bimodal mixing to be potentially detrimental, as they may decrease the ultimate tensile strength based on the material system (e.g., copper) due to inefficient inter-

layer binding. Chen et al. [23] did not observe any improvement with the bimodal distributions of stainless steel powders during powder spreading process as they hypothesize that percolation effect, which leads to particle segregation, had a strong impact on the overall process. Nevertheless, the authors recommended investigating different materials and different combinations of bimodal mixtures to evaluate the impact of powder size distributions on packing density. In summary, reported findings are primarily focused only on metallic materials which are produced via gas atomization and have highly different physical and morphological properties when compared with ceramics. Since binder jetting is extensively used in ceramics [32], there is a critical need for an investigation about the impact of multimodal distributions in ceramic feedstock during the powder spreading process.

This original research aims to quantitively investigate the fundamental impact of powder size distribution in ceramics on powder bed packing density, porosity, and flowability in a binder jetting process through DEM simulation techniques. Our empirical results validate that the use of bimodal sized distributions enhances the flowability and packing density of a powder spreading process. An increase in flowability between finer particles and bimodally distributed ones was reflected by a 49% reduction in the angle of repose between the finer size distributions used and the bimodal ones. In addition, an 8% increase in packing density was observed in the bimodal ceramic powder size distribution.

The rest of the paper is organized as follows. Section 2.2 describes an overview of the binder jetting process with a focus on the powder spreading and deposition mechanisms. Section 2.3 and 2.4 detail the material and selection of powder size distributions. In Section 2.5, the methodology and parameters used in the DEM simulations are presented. Section 2.6 highlights the major results and analysis from this study, along with a summary of major conclusions, limitations, and future direction for this research in Section 2.7.

2.2 Methods

2.2.1 Binder Jetting Process

This section details the binder jetting AM process shown in Figure **2-1**. First, a desired quantity of the powder is fed to the spreading roller (feed to powder ratio, referring to the thickness of feed layer to layer thickness, varies from 1 to 3) which evenly distributes a layer of powder across the powder bed in the build chamber. Subsequently, radiation from heat lamps is applied to remove moisture prior to binder deposition. Lastly, the array of nozzles in the printhead selectively deposits, i.e., jets droplets of binder onto the powder bed-based on the three-dimensional (3D) model of the printed part. This binder will act as an adhesive, joining the powder particles together due to surface tension created by the binder. This process is repeated layer by layer by lowering the build platform after each powder spread, until the final part is printed.

After the fabrication process is concluded, the part is carefully removed from the build platform acting as a “green part," which refers to the printed part's initial state without the final mechanical conditions achieved by post-AM processing [33]. Upon removal from the build platform, the "green part" undergoes de-powdering, curing, de-binding, sintering, consolidation, and infiltration [6], [33] depending on the build material, to achieve the final part properties. In contrast to most other materials, in the case of 3D sand-printing, the sand molds and cores produced via binder jetting can be used without any additional post-processing [34]–[36].

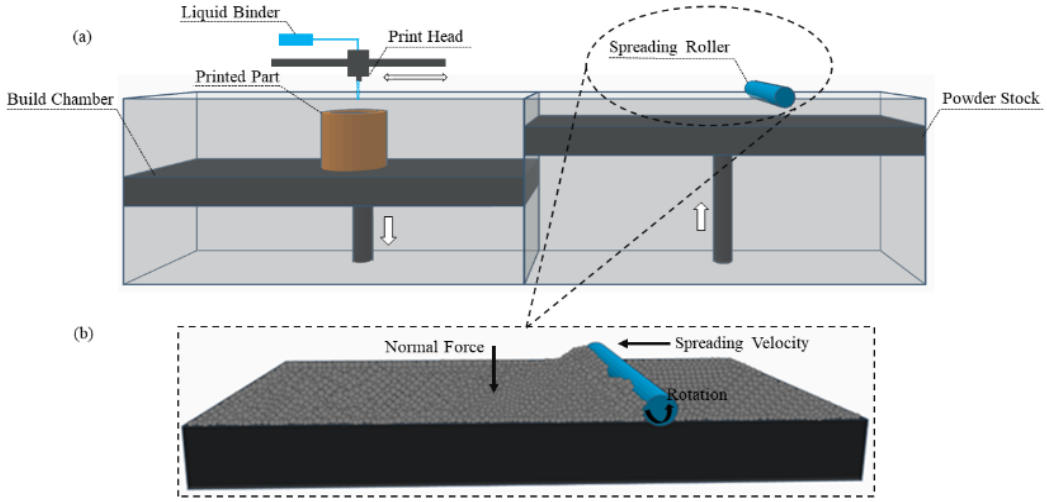

Figure **2-1**: a) Binder jetting additive manufacturing set-up. b) Forces in the powder spreading process.

2.2.2 Spreading and Deposition Mechanisms

In powder bed-based AM processes, the powder deposition and spreading stage plays an essential role in the layer's packing density, determining the final part's quality [22]. Based on a prior study, three types of deposition mechanisms have been identified in the powder spreading process [23]: namely, the wall effect, cohesion effect, and percolation effect which can be controlled to achieve a better packing density.

The wall effect influences the presence of cavities near the base plate during powder deposition in the initial several layers of the build process. As the powder is being spread, the roller acts as a wall restraining the free movement and deposition of particles [23], and is represented in Eq. (**2-1**) based on the volume ratio between the wall-particle cavities V_{w_p} and total cavities present V_T. Larger volume ratio indicates presence of stronger wall effects. The particle's diameter, roller diameter, and roller height are represented by d, D, and H, respectively:

$$V_{wp} = \frac{1}{6}\Pi^2\, dD\,\frac{D}{4} + H \tag{2-1}$$

$$V_T = 0.4\pi \frac{D^2}{4} \frac{H+1}{6\Pi^2 d} D \cdot \frac{D}{4+H}$$

where

$$\frac{V_{wp}}{V_T} = \frac{d\left(\frac{1}{H}+\frac{4}{D}\right)}{0.8+d\left(\frac{1}{H}+\frac{4}{D}\right)}$$

This study suggested that higher powder layer thickness could reduce the wall effect [23].

The cohesion effect due to Van der Waals forces causes agglomerations in the powder packing process before spreading. The simplified formula presented in Eq. (**2-2**), is used to evaluate the influence of Van der Waals forces. The ratio of Van der Waals forces between two spherical particles and gravity is represented by the bonding number, K [12].

$$K = \frac{3\pi\gamma}{8} d = \frac{9\gamma}{4\rho g} \cdot \frac{1}{d^2} \tag{2-2}$$

γ , d, ρ, and g represent the material's surface energy, particle diameter, material's density, and gravity respectively used for the calculations employed in the study. Since the bonding number is inversely proportional to the particle diameter, a decrease in particle size will result in higher Van der Waals forces, leading to particle agglomeration. It is recommended to identify an optimal particle size diameter that will lower K [23].

Finally, the percolation effect causes the powder particles to collide with each other as they pass through the moving powder bed in unimodal powder size distributions. In bimodal distributions, this effect could lead to powder segregation, since cavities could result from finer particles traveling faster than coarser particles in the powder bed.

Several process parameters are currently being investigated to improve the performance of binder jetting parts and reduce defects such as particle jamming, porosity, and formation of cavities

[25]. Another study has shown that applying a mechanical load such as normal stress on the powder, normal stress on the roller, and friction stress have an impact on the powder spreading process [6]. Chen et al. use DEM to evaluate the influence of particle contact stress and particle velocity in a powder spreading process [23]. Other studies have focused on the influence of particle size distributions and particle shape to understand their impact on the spreading process [24], [25], [37].

However, there is a major knowledge gap in the literature on the critical impact of the type of spreader, coupled with a rotational and translational speed, on the quality of powder deposition. Different powder-spreading methods are used to deposit the powder onto the baseplate, but the most common spreader systems are based on scrapers and rollers. A recent study by Cao et. al., illustrated the benefits of concurrently using both a counter-clockwise roller and a spreader [37]. In the study, the double smoothing method yielded better packing results and fewer part defects than a counter roller in finer particle size distributions.

Although a uniform powder layer is always desirable, it might not always be achievable in a spreading process. Results using a spreader speed of 100 mm/s have shown that in some cases, this non-uniformity does not directly affect the packing density of the bed [23].

Other studies based on particle spread simulations have used a counter-clockwise rotating roller to analyze the effect of spreading speed on powder bed. It was found that an increase in the roller's velocity will increase the surface roughness of the layers as well [26]. Finally, counter-rolling powder spreading with an increase in spreading speed resulted in a decrease in packing density and poor surface quality of the powder layers [22].

2.3 Materials

The feedstock material used in this research was powdered ceramic foundry sand, Cerabeads® consisting of Al2O3 61% and SiO2 36% [38]. The material was chosen for its

excellent manufacturing, mechanical, and chemical properties, and relevance for 3D Sand-Printing for sand-castings [35], [39]. The ceramic sand's spherical morphology offers an increase in flowability which directly impacts the quality of the powder bed [9].

Ceramic material has been growing in its applications across different industries such as automotive, oil and gas, mining, and construction because of its higher strength, higher heat resistance, improved part resolution, improved surface finish, reduced waste, stable grain size distribution, and high refractoriness [38]. Additional benefits that make this material ideal for binder jetting is its lower thermal expansion, high durability, and low thermal conductivity.

Although limited reported studies have focused on processing ceramic sand via AM technologies, few studies demonstrate the benefits of using binder jetting for rapid printing of sand-casting molds [40], [41] and other applications.

2.4 Powder Size

Based on specifications required for binder jetting of ceramic foundry sand, powder size distributions are selected to evaluate their performance on porosity, powder packing density, and flowability in the DEM simulation.

A prior study demonstrated the impact that particle size distribution has on achieving a high maximum packing density and uniform layer in a powder spreading process [24]. A ceramic sand's size distribution ranging from 50-109 μm and a powder bulk density of 1.69 g/cm^3 is chosen and grouped into different categories to analyze its effect on the spreading process, as shown in Table **2-1**. Ceramic foundry spherical particles are considered in this study because of their desired flowability properties and filling efficiencies [9], [38].

Table **2-1**: Particle size distributions classified into three groups.

Group	Particle Size Distribution (μm)	Mean Particle Size (μm)	St. Dev. of particle size (μm)
1	75-84	79.5	2.87
2	50+100	66	-
3	100-109	104.5	2.87

Three different groups corresponding to a range of powder sizes were selected for the analysis of results. Group 1 has a uniform distribution of powders ranging from 75-84 μm with a mean particle size of 79.5 μm. This group was selected because of the advantage of finer particles during sintering [9]. In group 2, a bimodal size distributions was achieved combining particles of 50 μm and 100 μm following a coarse to fine size ratio selection of 1:2 based on literature investigation [21], [23].

In recent years, there is a growing interest in quantifying the effect of unimodal or multimodal powder size distributions [9], [21], [24] in powder spreading processes in AM. The motivation for multimodal distributions lies in the postulation that it could increase powder packing density such that finer particles fill the voids created by coarser particles. This filling effect is presented in Figure **2-2** (finer particles in green fills the voids formed between the coarser particles in red). As the ratio of finer to coarser particles increases, it is necessary to avoid the loosening effect which refers to the overfilling of voids [17].

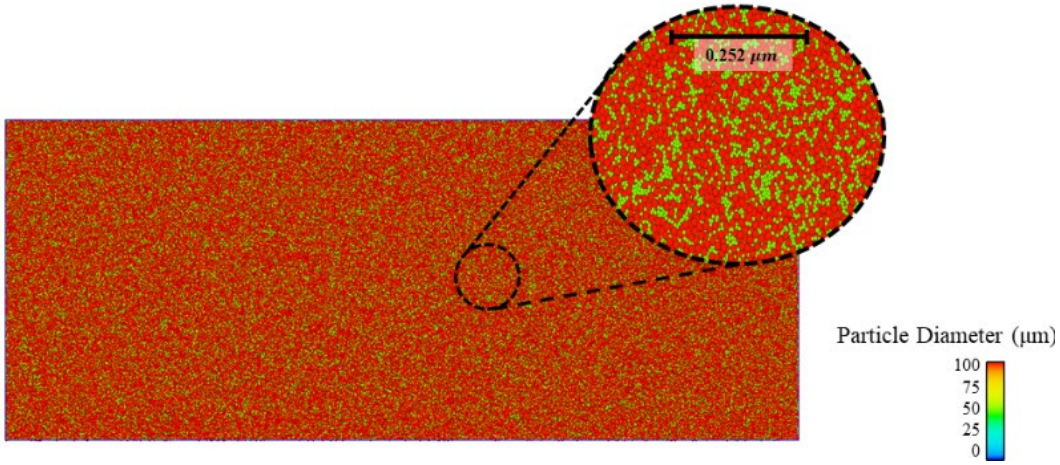

Figure **2-2**: Top view (xy plane) of the DEM generated powder bed illustrates the filling effect in bimodal powder distribution with coarser (100 μm in red) and finer (50 μm in green) particles.

This could increase powder bed layer density, flowability, and hence the green density of a printed part, [9], [17], [21]. However, determining an appropriate particle gradation is a necessary step prior to part fabrication which could be achieved by varying particle mixtures of finer to coarser ratios based on trial-and-error [42], a model-guided selection [9] , Furnas model [43], and linear packing models [44].

Group 3 has a uniform distribution of powders ranging from 100-109 μm with a mean value of 104.5 μm. The coarse particles were selected because of their favorable higher flowability. The layer height (μm) of each corresponding group is equal to about two times the largest powder size diameter (μm) of that group to ensure smooth spreading of the powder layer [23]. Groups 1, 2, and 3 have layer heights of 170, 200, and 220 μm, respectively.

2.5 Simulation

The DEM simulation setup, calculations, and parameters used are presented in this section.

2.5.1 Discrete-Element-Method

The powder spreading process in a binder jetting system (e.g., ExOne Innovent+) is simulated with FLOW-3D CFD software (Release 3 version, Flow Science, Santa Fe, NM, USA) based on DEM methodology. DEM is a numerical method to solve Newton's equations of

translational and rotational motion, by analyzing impact forces and dynamic interaction between powder particles by tracking the movements and inter-collisions of powder particles as discrete and rigid bodies.

The DEM solves the fundamental equation of motion represented in Eq. (**2-3**), where the force of particle *i* is calculated (mass of a solid particle m_i multiplied by the acceleration of a_i) for all contact forces due to particle interaction F_C and the external force, and gravity g. The sum of contact forces only corresponds to the particles in direct contact with the ith particle.

$$m_i a_i = \Sigma F_C + g \tag{2-3}$$

Since particle-particle interactions have multiple forces acting upon them, a spring-damper model is applied for the elastic forces and viscous dissipation based on the Voigt Model, which considers the contact in the normal and tangential direction. Eq. (**2-4**) is used to calculate the elastic force in DEM as a linear spring following Hooke's law, and elastic force F_e is calculated using a spring constant *k* and displacement δ.

Consequently, the displacement between particles δ_{ij} is calculated based on Eq. (**2-5**), with a distance L_{ij} between the center coordinates x_i and x_j of both interacting particles.

$$F_e = -k\delta \tag{2-4}$$

$$\delta_{ij} = L_{ij} - \left(r_i + r_j\right) \tag{2-5}$$

$$L_{ij} = \left\| x_i - x_j \right\|$$

The total force between particles in the DEM model F_i is calculated based on the sum of the forces in the normal direction F_n and in the tangential direction F_t as shown in Eq. (**2-6**).

$$F_i = F_n + F_t \tag{2-6}$$

$$F_n = -k_n \delta_{n_{ij}} - \eta_n u_{n_{ij}} \tag{2-7}$$

$$F_t = -\eta_t u_{t_{ij}} \tag{2-8}$$

In Eq. (**2-7**), the normal component F_n is calculated using k_n, $\delta_{n_{ij}}$, η_n, $u_{n_{ij}}$ which correspondingly represent the spring constant in the normal direction, the displacement between the solid particles *i* and *j*, the damping coefficient along the normal direction, and the relative velocity between solid particles *i* and *j*. In Eq. (**2-8**), the tangential component F_t uses η_t and $u_{t_{ij}}$ as the damping coefficient along the tangential direction, and the relative velocity between solid particles *i* and *j*.

2.5.2 Simulation Setup

The DEM simulation setup presented in Figure **2-3** is generated for a representative build box with corresponding length (4 cm), height (1.625 cm), and width (1.625 cm) in the *xyz* coordinate system. The boundaries of the model are treated as wall boundaries, with an exception at the outflow side (left end in Figure **2-3**) to allow for flow of particles to exit the system after spreading by a roller (4 cm in diameter and 0.25 cm in length) at a speed of 20 mm/sec. The dimensions in this DEM study mimic the build box of a commercially available binder jetting printer but are scaled down by a factor of 4 to lower computational costs.

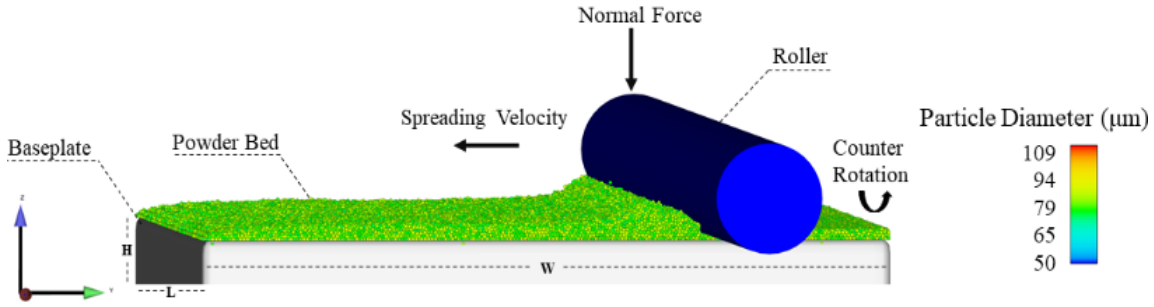

Figure **2-3**: Schematic of the powder spreading simulation setup (e.g., powder size distribution: 75-84 μm).

The simulation process begins with randomly generated particles that are settled into the print bed. After this, the spreading process begins with a counter-clockwise rotating roller that spreads the fine powder, to form a thin layer along the -y direction. The appropriate layer height utilized for each simulation group was calculated based on powder size as detailed in Section 2.4. The number of particles required for each simulation, based on their group number, (1-5) are calculated using Eq. (**2-9**), where P, v_d, and f are number of particles required in the simulation, domain volume, and packing fraction adjustment respectively.

$$P = \frac{v_d}{f} \tag{2-9}$$

Additional parameters used in the DEM simulation of a specific group are presented in Table **2-2**. The density of the material, Young's modulus, and Poisson's ratio correspond to the ceramic foundry sand studied. It should be noted that the coefficient of friction is critical in DEM studies since it directly impacts the dynamic behavior of powder particles [33].

Table **2-2**: Parameters used in the DEM simulation setup for a specific group.

Parameters	**Value**	**Unit**
Material's density (ρ) [38]	1.69	g/cm^3
Young's modulus (E)	1.55E+11	GPa
Poisson's ratio (η)	0.18	
Coefficient of restitution [45], [46]	0.9	
Friction coefficient [47] (dynamic, static)	(0.27, 0.19)	
Spring constant (k)	9.72E+01	
Gravity (g)	980	cm/s^2

The coefficient of restitution (COR) for this simulation was selected based on previous work [45], [46]. An investigation on the effect of the COR of silica sand [45] using different COR values yielded a value of 0.9 for the dry ceramic sand. The COR will increase at higher spreading velocity. Another study [46] that investigated glass spheres on vertical dispensing hoppers yielded similar results for COR value ranging from 0.9-0.94 for particle collisions.

During powder spreading process, an additional phenomenon that should be considered is slipping due to the contact boundary condition which imposes relative velocity between bodies in contact with each other. In this case, it is critical to account for this effect because of its impact on the quality of the spread layers and subsequently, the final print quality. Studies performed to improve layer quality have suggested that excessive slip can be avoided by inducing higher particle-wall frictions [48], [49].

The DEM model uses the simplified Hertz Mindlin model that includes nonlinear elasticity and slip [50], [51]. In this simulation study, two spring-damper models are created for normal contact between particle-wall interactions, and tangential (rolling friction) contact. In addition, slipping is accounted in the simulation setup. The parameter for slip ranges from 0 to 1 with 1 reflecting no slip on the contact surface [51], and every value in between displaying a partial slip with increasing effects along radial inward direction from the edge of the contact area, i.e. at slip-

stick region [51]. In this study, the parameters for partial slip are calculated from the particle-wall friction coefficient which accounts for the interaction between the powder and roller.

The spring constant k of the spherical shapes is calculated in Eq. (**2-10**) for all the three groups in this study. In this equation, $\rho, d, v,$ are the particle's density, maximum particle diameter in the corresponding group, and particle velocity that can be calculated with Eq. (**2-11**), respectively, where y is the moving distance.

$$k = 10\frac{\rho v^2 \pi d^3}{6\left(\frac{d}{2}\right)^2} \tag{2-10}$$

$$v = 2\sqrt{2gy} \tag{2-11}$$

2.6 Simulation Results and Discussion

In this section, the results from the DEM simulation are presented by highlighting the three critical powder spreading parameters studied to achieve higher quality in binder jetting AM parts.

2.6.1 Powder Packing Density and Porosity

The bulk volume and powder weight after spreading runs were used to estimate the powder packing density as shown in Figure **2-4**. A close-up view of the bounding box is presented at the top right of each figure to illustrate powder packing. The clearly visible piling on the powder bed in Figure **2-4** across all three groups at the same time stamp is caused by roller spreading, which is not presented for visualization.

In order to account for non-homogenous packing in the layers, three measurements of the packing density were taken per group size at different locations of the spread layer (Table **2-3**). Table **2-4** presents a one-way analysis of variance (ANOVA) as recommended by ASTM E2655. Referring to the calculated analysis of Figure **2-4**, there is a statistically significant influence of

powder size distribution in packing density at a 95% confidence interval. The average final powder packing densities of groups 1, 2, and 3 are 60%, 64%, and 59%, respectively. It is observed that a bimodal size distribution has an increase in packing density when compared to the unimodal sized groups. These results could be due to the benefit introduced with bimodal mixtures due to the filling effect, previously described, the agglomeration present in finer particles, and high wall effect that is present in larger particles.

Results from this study are in agreement with reported findings [21], where bimodal mixture increased the powder packing density by 8.2%. Bai et al. [30] also found an improvement on apparent (12.7%) and tap density (5.6%) with the introduction of the bimodal powder size distributions.

Table **2-3**: Powder packing densities measurements.

Groups	Count	Sum	Average	Variance
group 1	3	1.8	0.6	0.0004
group 2	3	1.92	0.64	0.0001
group 3	3	1.77	0.59	0.0004

Table **2-4**: ANOVA test of powder size distributions on packing density at 95% confidence level.

Source of Variation	SS	df	MS	F	p-value	F_{crit}
Between groups	0.0042	2	0.0021	7	0.027	5.143253
Within groups	0.0018	6	0.0003			
Total	0.006	8				

Porosity has often been associated with density in a powder spreading process [9]. It is a measure of void spaces that are created in the powder bed and is widely present in ceramic binder jetting [15]. Porosity (in percentage) of the powder layer is calculated using FlowSight (Particle STL converter software) and as expected, bimodal group 2 has the lowest porosity of 36%. Group

1 has a porosity of 40%, which is closer to the bimodal sized powder, and group 3 of 41%. This could be attributed to the formation of voids during particle-wall interactions between particle-print bed and particle-roller [48], [52] which causes agglomerations during the powder spreading process.

2.6.2 Powder Flowability

The angle of repose (AOR) as shown in Figure **2-5** is calculated at the same timestamp to measure flowability from the steepest angle of descent formed during the powder spreading process with respect to the previous layer. The AOR results achieved for group 1, group 2, and group 3 were 34.45°, 17.23°, and 13.14°, respectively. A smaller angle of repose has been shown to result in higher flowability [53]. It can be observed that although the coarser and bimodal powder sizes yield a lower angle of repose, the overall high flowability of the group sizes can be attributed to the spherical shape of the powder [21]. In addition, the use of only finer particles engage in a stronger cohesion effect during spreading which increases the Van der Waals forces and tends to form agglomerates with poor flowability [9], [24], [53]. Particle agglomeration was observed during the powder spreading of group 1 resulting in a higher AOR. Results obtained from Bai et al. agree with a powder flowability increase of 9.4% with a bimodal powder size distribution [21]. Overall, the results present a promising path for improving flowability during powder spreading in binder jetting AM process to achieve smooth and dense layers [21].

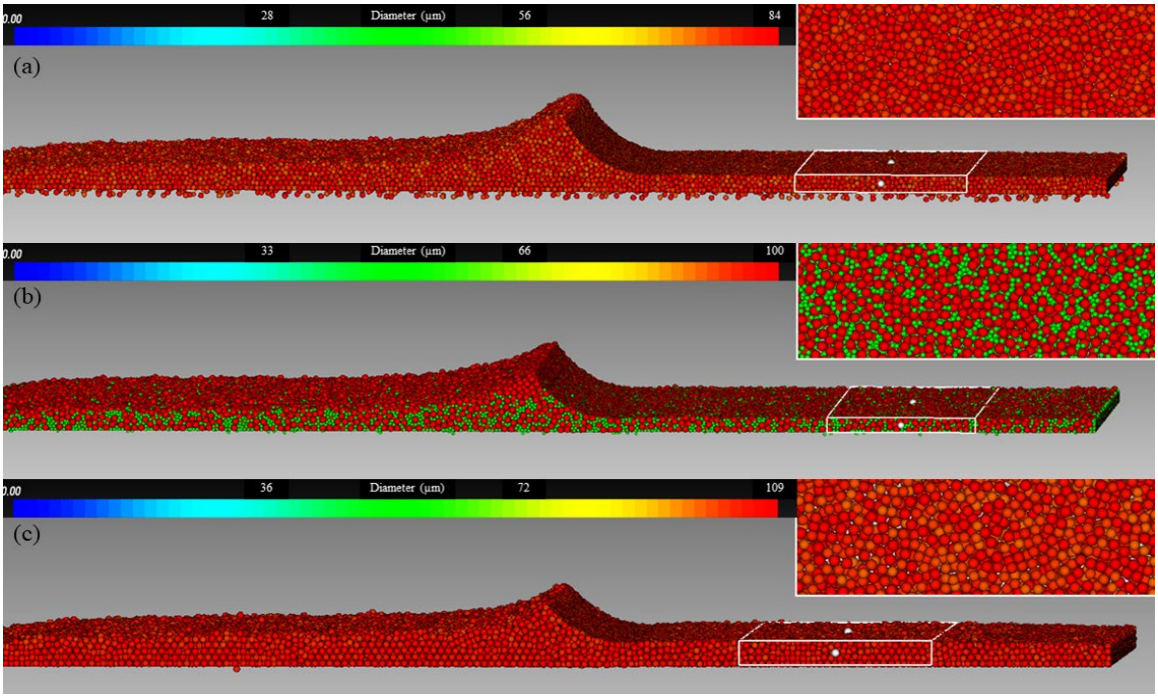

Figure **2-4**: Powder packing density at 0.53 seconds for powder size distributions: a) 75-84 µm b) 50+100 µm c) 100-109 µm.

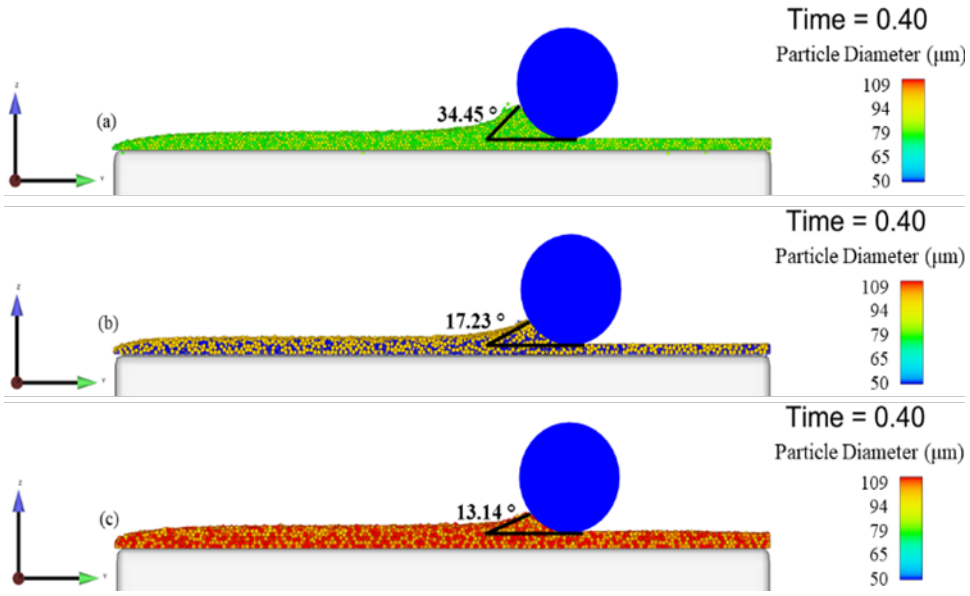

Figure **2-5**: Angle of repose at 0.40 seconds for powder size distributions: a) 75-84 µm b) 50+100 µm c) 100-109 µm.

2.7 Conclusion

Powder size distribution selection has a major influence on density and flowability. This paper presents a discrete-element-method (DEM) computational study to investigate packing density, powder bed porosity, and flowability of ceramic sand in binder jetting AM processes. Based on the results and analysis, we report the following major findings:

- Coarser particles have higher flowability values when compared with finer particles because of their lack of particle agglomeration. In turn, a finer particle distribution can be beneficial for higher packing density and sinterability.
- Bimodal size distribution can increase powder packing density and lower porosity.

Future work will include further exploration of the use of bimodal size distribution and selecting of different ratios of particle sizes to see the effect on the printed part's quality. Additionally, simulation work can be extended to evaluate the binder-powder interaction. Experimental validation is currently pursued by the authors using a binder jet (Innovent+) to investigate the underlying effect of cohesive response in bimodal particle distributions.

Acknowledgements

The author acknowledges the support from 2020 PA Manufacturing Fellows Initiative Grant, NSF CMMI award# #1944120, Flow Science, The Pennsylvania State University, and ExOne. Special thanks to Tess Zangrilli from Flow Science for her support.

References

[1] B. Mansfield, S. Torres, T. Yu, and D. Wu, "A Review on Additive Manufacturing of

Ceramics," *ASME 2019 14th Int. Manuf. Sci. Eng. Conf. MSEC 2019*, vol. 1, Nov. 2019, doi: 10.1115/MSEC2019-2886.

[2] E. O. Olakanmi, R. F. Cochrane, and K. W. Dalgarno, "A review on selective laser sintering/melting (SLS/SLM) of aluminium alloy powders: Processing, microstructure, and properties," *Progress in Materials Science*, vol. 74. Elsevier Ltd, pp. 401–477, Aug. 01, 2015, doi: 10.1016/j.pmatsci.2015.03.002.

[3] L. Yang and H. Miyanaji, "Ceramic additive manufacturing: a review of current status and challenges."

[4] T. D. Ngo, A. Kashani, G. Imbalzano, K. T. Q. Nguyen, and D. Hui, "Additive manufacturing (3D printing): A review of materials, methods, applications and challenges," *Composites Part B: Engineering*, vol. 143. Elsevier Ltd, pp. 172–196, Jun. 15, 2018, doi: 10.1016/j.compositesb.2018.02.012.

[5] S. A. Khairallah, A. T. Anderson, A. Rubenchik, and W. E. King, "Laser powder-bed fusion additive manufacturing: Physics of complex melt flow and formation mechanisms of pores, spatter, and denudation zones," *Acta Mater.*, vol. 108, pp. 36–45, Apr. 2016, doi: 10.1016/j.actamat.2016.02.014.

[6] G. Miao, W. Du, and Z. Pei, "Binder jetting additive manufacturing of ceramics: Analytical and numerical models for powder spreading process," in *ASME 2019 14th International Manufacturing Science and Engineering Conference, MSEC 2019*, Nov. 2019, vol. 1, doi: 10.1115/MSEC2019-2925.

[7] "ASTM E2655 - 14(2020) Standard Guide for Reporting Uncertainty of Test Results and Use of the Term Measurement Uncertainty in ASTM Test Methods." https://www.astm.org/Standards/E2655.htm (accessed Feb. 14, 2021).

[8] Z. C. Eckel, C. Zhou, J. H. Martin, A. J. Jacobsen, W. B. Carter, and T. A. Schaedler, "Additive manufacturing of polymer-derived ceramics," *Science (80-.).*, vol. 351, no. 6268,

pp. 58–62, Jan. 2016, doi: 10.1126/science.aad2688.

[9] W. Du, X. Ren, Z. Pei, and C. Ma, “Ceramic Binder Jetting Additive Manufacturing: A Literature Review on Density,” *J. Manuf. Sci. Eng.*, vol. 142, no. 4, Apr. 2020, doi: 10.1115/1.4046248.

[10] S. Gopagoni *et al.*, “Microstructural evolution in laser deposited nickel-titanium-carbon in situ metal matrix composites,” *J. Alloys Compd.*, vol. 509, no. 4, pp. 1255–1260, Jan. 2011, doi: 10.1016/j.jallcom.2010.09.208.

[11] D. B. Miracle, “Metal matrix composites - From science to technological significance,” *Compos. Sci. Technol.*, vol. 65, no. 15-16 SPEC. ISS., pp. 2526–2540, Dec. 2005, doi: 10.1016/j.compscitech.2005.05.027.

[12] R. Galante, C. G. Figueiredo-Pina, and A. P. Serro, “Additive manufacturing of ceramics for dental applications: A review,” *Dental Materials*, vol. 35, no. 6. Elsevier Inc., pp. 825–846, Jun. 01, 2019, doi: 10.1016/j.dental.2019.02.026.

[13] J. E. Nevelos, E. Ingham, C. Doyle, A. B. Nevelos, and J. Fisher, “The influence of acetabular cup angle on the wear of ‘BIOLOX Forte’ alumina ceramic bearing couples in a hip joint simulator,” *J. Mater. Sci. Mater. Med.*, vol. 12, no. 2, pp. 141–144, 2001, doi: 10.1023/A:1008970027306.

[14] W. Höland, M. Schweiger, R. Watzke, A. Peschke, and H. Kappert, “Ceramics as biomaterials for dental restoration,” *Expert Rev. Med. Devices*, vol. 5, no. 6, pp. 729–745, Nov. 2008, doi: 10.1586/17434440.5.6.729.

[15] X. He, Y. Z. Zhang, J. P. Mansell, and B. Su, “Zirconia toughened alumina ceramic foams for potential bone graft applications: Fabrication, bioactivation, and cellular responses,” in *Journal of Materials Science: Materials in Medicine*, Jul. 2008, vol. 19, no. 7, pp. 2743–2749, doi: 10.1007/s10856-008-3401-x.

[16] Y. Hu and W. Cong, “A review on laser deposition-additive manufacturing of ceramics and

ceramic reinforced metal matrix composites," *Ceramics International*, vol. 44, no. 17. Elsevier Ltd, pp. 20599–20612, Dec. 01, 2018, doi: 10.1016/j.ceramint.2018.08.083.

[17] W. Du, X. Ren, Y. Chen, C. Ma, M. Radovic, and Z. Pei, "Model guided mixing of ceramic powders with graded particle sizes in binder jetting additive manufacturing," in *ASME 2018 13th International Manufacturing Science and Engineering Conference, MSEC 2018*, Sep. 2018, vol. 1, doi: 10.1115/MSEC2018-6651.

[18] S. Haeri, Y. Wang, O. Ghita, and J. Sun, "Discrete element simulation and experimental study of powder spreading process in additive manufacturing," *Powder Technol.*, vol. 306, pp. 45–54, Jan. 2017, doi: 10.1016/j.powtec.2016.11.002.

[19] G. Manogharan, M. Kioko, and C. Linkous, "Binder Jetting: A Novel Solid Oxide Fuel-Cell Fabrication Process and Evaluation," *JOM*, vol. 67, no. 3, pp. 660–667, Mar. 2015, doi: 10.1007/s11837-015-1296-9.

[20] S. Shrestha and G. Manogharan, "Optimization of Binder Jetting Using Taguchi Method," vol. 69, doi: 10.1007/s11837-016-2231-4.

[21] Y. Bai, G. Wagner, and C. B. Williams, "Effect of particle size distribution on powder packing and sintering in binder jetting additive manufacturing of metals," *J. Manuf. Sci. Eng. Trans. ASME*, vol. 139, no. 8, Aug. 2017, doi: 10.1115/1.4036640.

[22] H. Chen, Y. Chen, Y. Liu, Q. Wei, Y. Shi, and W. Yan, "Packing quality of powder layer during counter-rolling-type powder spreading process in additive manufacturing," *Int. J. Mach. Tools Manuf.*, vol. 153, p. 103553, Jun. 2020, doi: 10.1016/j.ijmachtools.2020.103553.

[23] H. Chen, Q. Wei, Y. Zhang, F. Chen, Y. Shi, and W. Yan, "Powder-spreading mechanisms in powder-bed-based additive manufacturing: Experiments and computational modeling," *Acta Mater.*, vol. 179, pp. 158–171, Oct. 2019, doi: 10.1016/j.actamat.2019.08.030.

[24] W. Nan, M. Pasha, and M. Ghadiri, "Numerical simulation of particle flow and segregation

during roller spreading process in additive manufacturing," *Powder Technol.*, vol. 364, pp. 811–821, Mar. 2020, doi: 10.1016/j.powtec.2019.12.023.

[25] W. Nan *et al.*, "Jamming during particle spreading in additive manufacturing," *Powder Technol.*, vol. 338, pp. 253–262, Oct. 2018, doi: 10.1016/j.powtec.2018.07.030.

[26] E. J. R. Parteli and T. Pöschel, "Particle-based simulation of powder application in additive manufacturing," *Powder Technol.*, vol. 288, pp. 96–102, Jan. 2016, doi: 10.1016/j.powtec.2015.10.035.

[27] Y. Lee, A. K. Gurnon, D. Bodner, and S. Simunovic, "Effect of Particle Spreading Dynamics on Powder Bed Quality in Metal Additive Manufacturing," *Integr. Mater. Manuf. Innov.*, vol. 9, no. 4, pp. 410–422, Dec. 2020, doi: 10.1007/s40192-020-00193-1.

[28] Y. S. Lee, P. Nandwana, and W. Zhang, "Dynamic simulation of powder packing structure for powder bed additive manufacturing," *Int. J. Adv. Manuf. Technol.*, vol. 96, no. 1–4, pp. 1507–1520, Apr. 2018, doi: 10.1007/s00170-018-1697-3.

[29] W. Du, M. Singh, and D. Singh, "Binder jetting additive manufacturing of silicon carbide ceramics: Development of bimodal powder feedstocks by modeling and experimental methods," *Ceram. Int.*, vol. 46, no. 12, pp. 19701–19707, Aug. 2020, doi: 10.1016/J.CERAMINT.2020.04.098.

[30] Y. Bai, G. Wagner, and C. B. Williams, "Effect ofBimodal Powder Mixture on Powder Packing Density and Sintered Density in Binder Jetting of Metals."

[31] H. Miyanaji, K. M. Rahman, M. Da, and C. B. Williams, "Effect of fine powder particles on quality of binder jetting parts," *Addit. Manuf.*, vol. 36, p. 101587, Dec. 2020, doi: 10.1016/j.addma.2020.101587.

[32] A. Mostafaei *et al.*, "Binder jet 3D printing – Process parameters, materials, properties, and challenges," *Progress in Materials Science*. Elsevier Ltd, p. 100707, Jun. 15, 2020, doi: 10.1016/j.pmatsci.2020.100707.

[33] Y. Zhang, W. Jarosinski, Y. G. Jung, and J. Zhang, "Additive manufacturing processes and equipment," in *Additive Manufacturing: Materials, Processes, Quantifications and Applications*, Elsevier, 2018, pp. 39–51.

[34] P. Lynch, C. Hasbrouck, J. Wilck, M. Kay, and G. Manogharan, "Challenges and opportunities to integrate the oldest and newest manufacturing processes: metal casting and additive manufacturing," *Rapid Prototyp. J.*, vol. 26, no. 6, pp. 1145–1154, Jun. 2020, doi: 10.1108/RPJ-10-2019-0277.

[35] D. Martinez, C. Bate, and G. Manogharan, "Towards Functionally Graded Sand Molds for Metal Casting: Engineering Thermo-mechanical Properties Using 3D Sand Printing," *JOM*, vol. 72, no. 3, pp. 1340–1354, Mar. 2020, doi: 10.1007/s11837-019-03975-x.

[36] P. King, D. Martinez, and G. P. Manogharan, "Novel Sprue Designs to Reduce Casting Defects in Nickel-Aluminum Bronze: A Computational Study," Sep. 2020, doi: 10.1115/msec2020-8486.

[37] S. Cao, Y. Qiu, X. F. Wei, and H. H. Zhang, "Experimental and theoretical investigation on ultra-thin powder layering in three dimensional printing (3DP) by a novel double-smoothing mechanism," *J. Mater. Process. Technol.*, vol. 220, pp. 231–242, Jun. 2015, doi: 10.1016/j.jmatprotec.2015.01.016.

[38] "Naigai cerabeads® 60 : products - Itochu Ceratech corp." http://www.itc-cera.co.jp/english/prod/index.html (accessed Nov. 17, 2020).

[39] S. R. Sama, T. Badamo, and G. Manogharan, "Case Studies on Integrating 3D Sand-Printing Technology into the Production Portfolio of a Sand-Casting Foundry," *Int. J. Met.*, vol. 14, no. 1, pp. 12–24, Jan. 2020, doi: 10.1007/s40962-019-00340-1.

[40] M. Upadhyay, T. Sivarupan, and M. El Mansori, "3D printing for rapid sand casting—A review," *Journal of Manufacturing Processes*, vol. 29. Elsevier Ltd, pp. 211–220, Oct. 01, 2017, doi: 10.1016/j.jmapro.2017.07.017.

[41] J. Thiel, S. Ravi, and N. Bryant, “Advancements in materials for three-dimensional printing of molds and cores,” *Int. J. Met.*, vol. 11, no. 1, pp. 3–13, Jan. 2017, doi: 10.1007/s40962-016-0082-y.

[42] C. Sun *et al.*, “Effect of particle size gradation on the performance of glass-ceramic 3D printing process,” *Ceram. Int.*, vol. 43, no. 1, pp. 578–584, Jan. 2017, doi: 10.1016/j.ceramint.2016.09.197.

[43] J. Zheng, W. B. Carlson, and J. S. Reed, “The packing density of binary powder mixtures,” *J. Eur. Ceram. Soc.*, vol. 15, no. 5, pp. 479–483, Jan. 1995, doi: 10.1016/0955-2219(95)00001-B.

[44] T. Stovall, F. de Larrard, and M. Buil, “Linear packing density model of grain mixtures,” *Powder Technol.*, vol. 48, no. 1, pp. 1–12, Sep. 1986, doi: 10.1016/0032-5910(86)80058-4.

[45] J. Ge and C. A. Monroe, “The Effect of Coefficient of Restitution in Modeling of Sand Granular Flow for Core Making: Part I Free-Fall Experiment and Theory,” *Int. J. Met.*, vol. 13, no. 4, pp. 753–767, Oct. 2019, doi: 10.1007/s40962-019-00333-0.

[46] A. Anand, J. S. Curtis, C. R. Wassgren, B. C. Hancock, and W. R. Ketterhagen, “Predicting discharge dynamics from a rectangular hopper using the discrete element method (DEM),” *Chem. Eng. Sci.*, vol. 63, no. 24, pp. 5821–5830, Dec. 2008, doi: 10.1016/j.ces.2008.08.015.

[47] “Coefficients of Friction between Calcareous Sands and Some Building Materials, and Their Significance.” https://apps.dtic.mil/sti/citations/ADA066297 (accessed Feb. 28, 2021).

[48] C. Meier, R. Weissbach, J. W einberg, W. A. Wall, and A. J. Hart, “Critical influences of particle size and adhesion on the powder layer uniformity in metal additive manufacturing,” *J. Mater. Process. Technol.*, vol. 266, pp. 484–501, Apr. 2019, doi: 10.1016/j.jmatprotec.2018.10.037.

[49] Y. Ma, T. M. Evans, N. Philips, and N. Cunningham, “Numerical simulation of the effect

of fine fraction on the flowability of powders in additive manufacturing," *Powder Technol.*, vol. 360, pp. 608–621, Jan. 2020, doi: 10.1016/j.powtec.2019.10.041.

[50] Y. Lee, S. Simunovic, and A. K. Gurnon, "Quantification of Powder Spreading Process for Metal Additive Manufacturing," 2019. Accessed: Feb. 17, 2021. [Online]. Available: http://www.osti.gov/scitech/.

[51] B. Yan, R. A. Regueiro, and S. Sture, "Three-dimensional ellipsoidal discrete element modeling of granular materials and its coupling with finite element facets," *Eng. Comput. (Swansea, Wales)*, vol. 27, no. 4, pp. 519–550, Jan. 2010, doi: 10.1108/02644401011044603.

[52] M. Y. Shaheen, A. R. Thornton, S. Luding, and T. Weinhart, "The influence of material and process parameters on powder spreading in additive manufacturing," *Powder Technol.*, vol. 383, pp. 564–583, May 2021, doi: 10.1016/j.powtec.2021.01.058.

[53] G. Miao, W. Du, M. Moghadasi, Z. Pei, and C. Ma, "Ceramic binder jetting additive manufacturing: Effects of granulation on properties of feedstock powder and printed and sintered parts," *Addit. Manuf.*, vol. 36, p. 101542, Dec. 2020, doi: 10.1016/j.addma.2020.101542.

Chapter 3

Bimodal Particle Size Distributions in 316L Stainless Steel Binder Jetting and the Impact on Density and Mechanical Performance

This Chapter is planned for submission for publication at JOM: A. Paula Clares, R. Stebbins, G. Manogharan (2022). Bimodal Particle Size Distributions in 316L Stainless Steel Binder Jetting and the Impact on Density and Mechanical Performance.

Abstract

Binder jetting is an additive manufacturing (AM) technology that has gained popularity and attention in recent years. It relies on powder feedstock to fabricate parts without the need of an energy source to melt the material during the layer by layer build up. This avoids melting, residual stresses, and rapid solidification defects within parts. Because of this, binder jetting has become an attractive alternative for metal materials. However, one of the greatest drawbacks of this technology is the low relative densities produced. The authors present the use of bimodal powder size distributions (a mixture of coarse to fine particles) as a method for increasing part density. This work focuses on investigating the impact that SS316L bimodal mixtures have on sintered density and mechanical performance. Four unimodal and two bimodal groups were selected for sintered density measurements and three-point bend testing. Results found that when compared to some of the unimodal groups, bimodal size distributions showed a statistically higher sintered density, and a 20.18% and 19.74% increase when compared with the highest unimodal density achieved. It was also found that the Ultimate Flexural Strength (UFS) achieved with the bimodal groups yielded an increase of 168.3% and 173.4% when compared to the highest performing unimodal group.

3.1 Introduction

Binder jetting was developed at MIT in the early 1990s and is one of the seven additive manufacturing (AM) technologies available. Similar to Direct Energy Deposition (DED) and Laser Powder Bed Fusion (LPBF), this technology relies on powder as feedstock for the fabrication of parts. The process begins with powder dispensing, and depending on the binder jetting system, a rake, blade, or rotating roller is used to spread a thin layer of that powder into the build chamber. Next, the binder is deposited with an array of nozzles that eject the solution into the powder bed. The droplets selectively bond the powder particles based on the computer-aided design (CAD) file that is used to guide the printing. This process is repeated layer by layer until a final part is achieved. At this stage, the geometry is known as a "green part" displaying low mechanical properties. Upon build completion, post-processing steps such as curing, depowering, sintering, material infiltration, and finishing are necessary to achieve a final densification and a fully functioning part.

Binder jetting offers multiple advantages over other AM technologies, such as eliminating the need for support structures, powder reusability, and part nesting. In contrast to other powder AM technologies, binder jetting does not use any energy source (e.g., laser or electron beam) during the fabrication process and therefore evades melting and rapid solidification defects, as well as residual stresses accumulated on the fabricated parts [1]. Because of this, binder jetting is regarded as a very flexible AM technique that can process a wide range of materials, such as sand, ceramics, polymers, and metals [1].

Metal binder jetting is considered a promising alternative to traditional manufacturing methods and has gained particular interest over the years for its ability to fabricate complex geometries and designs quicker, at larger volumes, and lower machine and production costs [2]. The lack of distortions introduced to the part due to the absence of thermal gradients during the build up process, and lack of thermal crack formations, makes this technology attractive for

continuous industrial applications. Even though the number of materials studied in binder jetting is low when compared to LPBF and DED, in recent years, the investigations have been increasing [3].

Despite the high popularity in metal binder jetting, especially for optically reflective and thermally conductive metals [4], one of the main and most detrimental drawbacks of this technology is the relatively low densities of printed parts (or high porosity) when compared to fabrications through powder metallurgy or other metal AM processes [5]. Binder jetting as-built (green stage) parts are typically brittle, porous, and possessing poor mechanical properties [6]. Previous work reports average relative green densities of around 40-60% in binder jetting fabrications [6]–[8]. Efforts have been made to increase the overall printed part's density such as post-processing, hot isostatic pressing (HIP), optimization of printing process parameters, and powder properties [5]. Post-processing steps such as material infiltration have demonstrated effectiveness in increasing density. For example, Vogt et al., reported a 26.7% increase from the green density after ceramic slurry infiltration [9] while Porter et al. calculated a 65% density improvement when compared to green parts during the fabrication of Al-based metal matrix nanocomposites [10]. Kumar et. al demonstrated that using the HIP technique, a maximum density of 97.32% and 92% in copper parts could be achieved [11], [12]. Finally, in a different study, Dahmen et. al., achieved close to full densification with HIP on a nickel-base superalloy [13]. Optimization of binder jetting process parameters have been studied as well for density improvement. Shrestha et al. analyze the impact of several process parameters (binder saturation, layer thickness, and feed-to-powder ratio) on SS316L, concluding with an optimal selection to enhance density [14]. Lecis et. al looked at the influence of layer thickness, binder saturation, as well as debinding and sintering atmospheres in SS316L, achieving final densities above 98% [2].

Although research has investigated a range of options to improve either in sintered or green density, the focus of this work lies on the effects of powder properties, specifically powder size

distribution. The evolution of this strategy can be traced back to powder metallurgy research that recognized that the introduction of bimodal powder mixtures can improve packing density and lead to better dimensional control after sintering [15], [16]. In the aforementioned phenomena, both coarse and fine particles are mixed (usually at around 1:3-1:6 size ratios) for an increase in packing density through the so-called filling effect [17]. This effect describes the filling of fine particles into the voids created between the coarse particles as they pack. The effect of bimodal powder distributions in ceramics has been experimentally investigated in the past couple of years. Du et al. looked at the use of bimodal spherical powder feedstocks in silicon carbide ceramics to achieve a 5% increase in green density when compared to unimodal powder prints [16]. In later work, Du et al. used spherical alumina powders to demonstrate the improvement of powder bed density and sintered density when working with bimodal mixtures [18]. That investigation also focused on the use of an analytical model to find the optimal mixing fraction.

Metal bimodal powder size distributions have also been investigated in literature. In [15], Bai et al. experimentally evaluated the effect of bimodal mixture copper parts, observing an increase of 16.2 % in packing density and 12.3% in sintered density, depending on the variation of sinter conditions. In [19], Bai et al. study the impact of copper bimodal mixtures resulting in an 8.2% improvement in powder packing density, and a 4% increase in sintered density. Sinterability and density improvements in SS316L printed parts were studied by Batmaz et. al., [20] finding that the bimodal size distribution group led to optimum printing/sintering characteristics.

Even though the impact of bimodal distributions in green and sintered densities has been well studied for other metal materials, there is still a need to understand the effect of bimodal particle size distribution in SS316L binder jetting and the impact on sintered density and mechanical performance. The motivation of this paper is to experimentally validate the benefits bimodal mixtures offer, and using different SS316L powder size distributions, evaluate the impact this has in sintered density and *mechanical performance*. This paper is a continuation of previous

computational work based on the discrete-element-method (DEM) and the effects of particle size distributions in packing density, porosity, and flowability [21].

Section 2 describes the experimental methods conducted with a focus on material selection, powder characterization, part fabrication and printing parameters used, as well as post-processing. Section 3 focuses on the part evaluation techniques utilized. Sections 4 and 5 detail on the results obtained in this study and discusses their implications. Finally, Section 6 highlights the major findings and explains the need for future work.

3.2 Experimental Methods

3.2.1 Material Selection

Nitrogen gas atomized (SS316L) 316L stainless steel powder was chosen for experiment fabrication. In order to achieve specific powder size distributions, two powder manufacturers, Sandvik (Stockholm, SE), and Carpenter Additive (Philadelphia, USA) were selected. To ensure similar chemical compositions, a sample from each batch (500 mg) was analyzed for total C, S, O, N, and H content. An examination was conducted using ELEMENTRAC ONH-p 2 and ELEMENTRAC CS-I (ELTRA, USA) equipment. O%, N%, and H% content was extracted in triplicate via inert gas fusion technique, while combustion was used for C% and S% concentration. In Table **3-1**, element analysis results display a comparable chemical composition between both powders except O% and H%. Slight oxidation of the powder (as observed in Sandvik) has demonstrated to improve powder flowability. Because the sintering processing in this work is enclosed in completely inert gas, the O% differences between manufacturers does not play a role in results and only play a role in powder spreading. Natural oxidation of powder is often present in binder jetting with powder reusability.

Table **3-1**: Chemical composition of as sourced SS316L powders (500 mg).

Powder Manufacturer	C%	S%	O%	N%	H(ppm)
Carpenter Additive	.014	.005	.040	.090	5.490
Sandvik Osprey	.013	.004	.149	.145	16.720

3.2.2 Powder Characterization

To evaluate the impact of powder size distribution on fabricated binder jetting parts, six powder size groups with different size distributions were prepared using a vibratory sieve (Retsch AS 200 Control, Haan DE) and different mesh sizes. As shown in Table **3-2**, these groups are made of four unimodal and two bimodal size distributions to compare the difference in density and mechanical performance.

Table **3-2:** Powder size groups (μm).

	Groups	D10	D50	D90
Unimodal Distribution	10 μm	5.3	12.5	22.6
	20 μm	16.3	22.1	29.8
	30 μm	22.1	31.3	41.8
	40 μm	25.7	36.4	48.3
Bimodal Distribution	30 (73% weight)+10 μm	10.6	26.8	39.0
	40 (73% weight)+10 μm	10.7	32.7	47.4

Using Dynamic Image Analysis (DIA) technique through Microtrac MRB- CAMSIZER X2 equipment (Newtown, PA), particle size distribution and morphology were measured following the ISO 13322-2 standard [22]. As shown in Figure **3-1**a, median particle size (D50) values for unimodal groups are around 12 μm, 22 μm, 31 μm, and 36 μm for groups 1, 2, 3, and 4. Groups 5 and 6, consist of a bimodal particle size distributions which is a combination of coarse and fine particles. Based on literature work, a size ratio of 1:3-1:4 is ideal for bimodal mixtures, while a weight ratio of 73-27 % has been reported to maximize powder packing density [19]. For groups 5

and 6, the powder was prepared by weighing and mixing for 2 hours using a 3D shaker (Turbula-WAB Group, CH).

Finally, Figure **3-1**b displays powder morphology obtained at 0.8 µm per pixel, showing high sphericity in the SS316L stainless steel powder that was used for this work. Low surface defects and satellites were observed as well, which can be beneficial for powder flowability, as the aforementioned defects can create angularity in powder.

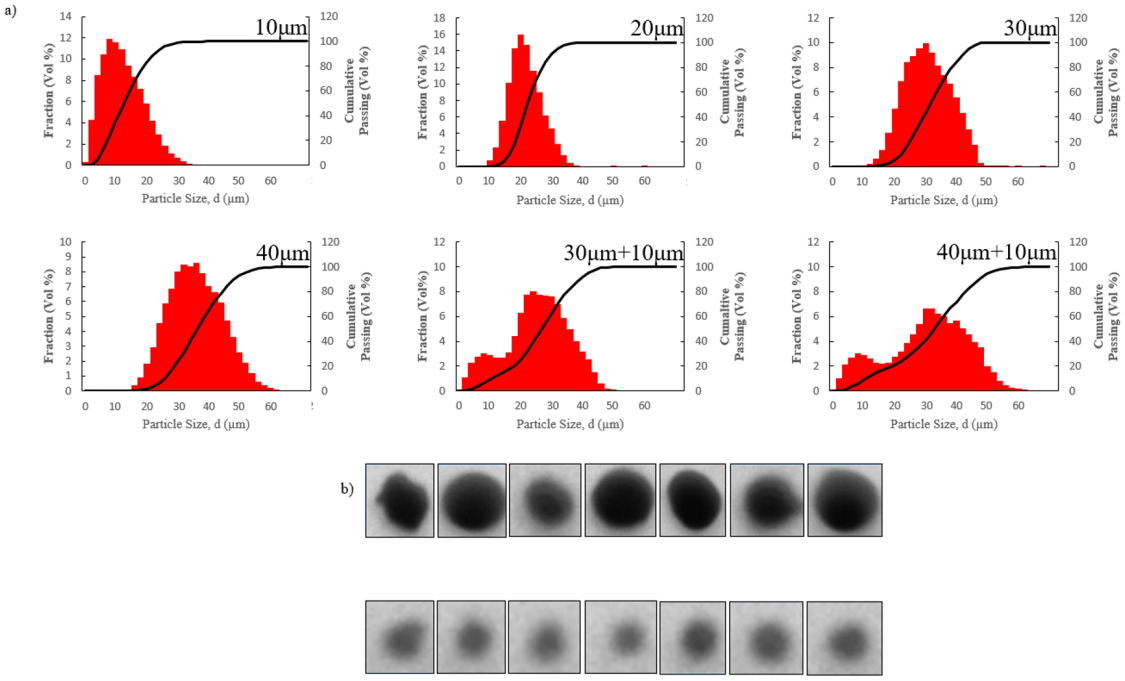

Figure **3-1**: a) Powder size distributions of SS316L groups. b) Powder morphology images (0.8 µm per pixel).

3.2.3 Part Fabrication and Printing Parameters

An ExOne (North Huntingdon, PA) Innovent+ binder jetting machine was used for the fabrication of all parts. BA005 aqueous-based binder (supplied by ExOne) was selected which uses polyvinylpyrrolidone (PVP) polymer as a bonding agent. A total of six builds were printed corresponding to each powder size group. To evaluate and compare the mechanical strength of the unimodal and the bimodal printed samples, 31.7 mm x 12.7 mm x 6.35 mm bars were designed in

SolidWorks following the ASTM B528-99 standard. To evaluate sintered density in the binder jetting fabricated parts (unimodal vs bimodal), 7 mm (D) x 20 mm (L) cylinders were printed. An example of the green parts printed from the 10 µm group size is shown in Figure **3-2**.

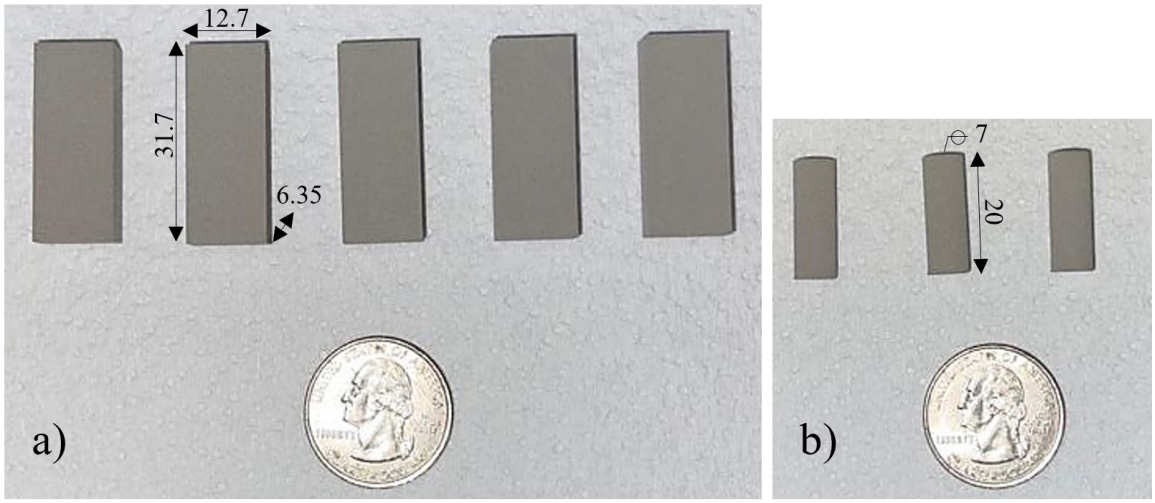

Figure **3-2**: Example of green 10 µm group size samples. a)Bars (mm) and b)Cylinders (mm).

Given that build layout can affect the density and mechanical performance of printed parts, a total of five bars and four cylinders were printed per build and placed in different locations. The bars were fabricated perpendicular to the load direction within the build platform, as shown in Figure **3-3**.

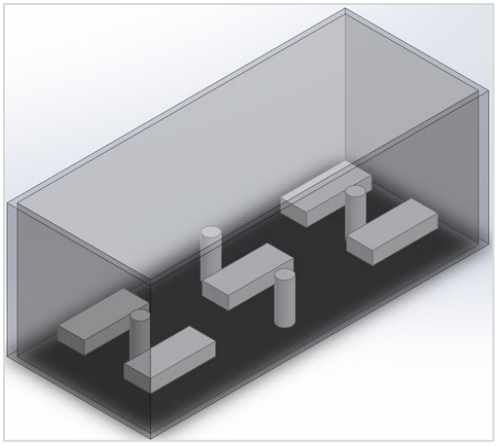

Figure **3-3**: Build layout for each powder size group.

Table **3-3** provides an overview of the process parameters that were utilized for the AM fabrication of all SS316L samples. Studies describe how different process-related parameters might affect a final part [14], [23]. For this investigation, all parameters were kept consistent when possible. This was done in order to have powder size distribution as the only major varying parameter. Layer thickness varied slightly across groups, as this is a variable directly related to the powder size. It is recommended that the thickness of the layers should be around three times the particle diameter for higher packing density and a smooth surface finish [24]. Another parameter that slightly changed across groups was the recoat speed, which is the speed at which the hopper traverses the build while dispensing powder [25]. After observation, a lower speed (mm/s) was utilized for finer particles because of the difficulty in powder dispensing due to clumping and agglomeration. Additionally, bed drying time, which is the time the heat lamp takes to pass over the deposited binder for drying, was adjusted between groups as different particle sizes varied this parameter. Observations in respect to part bleeding and layer delamination guided the adjustment of the bed drying time values.

Table **3-3**: Printing process parameters.

Parameter	**10 µm**	**20 µm**	**30 µm**	**40 µm**	**30 (73%)+10 µm**	**40(73%)+10 µm**
Layer Thickness(µm)	100 -115					
Desired Saturation (%)	65					
Rotation Speed (rpm)	500					
Traverse Speed (mm/s)	3					
Recoat Speed (mm/s)	30		60			
Bed Temperature (°C)	55					
Bed Drying Time (s)	5		10		5	

3.2.4 Post-Processing

After green part fabrication, all samples were cured following ExOne's recommendation at 200 °C for 5 hours after printing, for an increase in green part strength. Manual depowering and removal from the build box followed. Finally, all samples were sintered in an Argon inert gas atmosphere. A tube furnace (Carbolite Gero Ltd.) was used with the following temperature profile: **(I)** 3 °C/min ramp to 700 °C, 60 min dwell; **(II)** 3 °C/min ramp to 1120 °C, 140 min dwell; **(III)** cool down at 3 °C/min to 850 °C, 90 min and to 300 °C, 183 min; and **(IV)** cool down at 3°C/min to room temperature. A similar sinter cycle can be observed on previous SS316L binder jetting work [14]. In Figure **3-4**, the heat temperature profile used for the sintering process is shown. The bottom arrows indicate where the debinding (binder burn out) takes place followed by the sintering (full part densification).

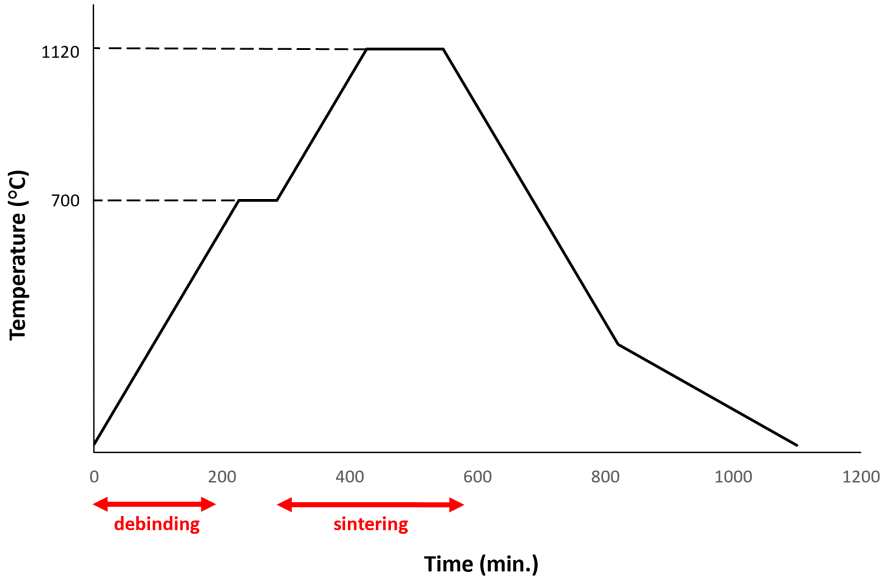

Figure **3-4**: Heat temperature profile used for sintering SS316L samples.

3.3 Part Evaluation Techniques

3.3.1 Sintered Density

Sintered density was measured for all cylinder samples from each group (n=4). Density measurements were made using a digital caliper (10 μm accuracy) for the cylinder dimensions, and a digital scale (0.1 mg) for weight recordings. Upon visual inspection, diameter uniformity was assumed throughout the length of the cylinder, and it was measured from the top and bottom. In Eq. (**3-1**), the formula used for caliper density calculations is shown where $m_{cylinder}$ is the total mass of the cylinder and $v_{cylinder}$ is the volume using the radius and height of the cylinder. This value was later divided by the theoretical density of SS316L stainless steel (8.00 g/cm3) for relative density percent present in the printed part.

$$\rho_{sintered} = \frac{m_{cylinder}}{v_{cylinder}} \tag{3-1}$$

Upon collecting sintered data from all printed samples (n=4 per group), a more precise measurement of density was further explored using X-ray computed tomography (XrCT) on only one cylinder sample per group size (n=1). This technique was selected as it is a noninvasive tool that enables the evaluation of internal features of printed parts. A GE Vtomex L300 CT scanner with a microfocus tube was used. Scans were collected using a 250 kV 40 μA X-ray beam with 10 μm voxel resolution. Raw XrCT data was collected as 16-bit tiff stack files and imported for processing into Image J software where cleaning, cropping, and gray scale adjustment was done. AVIZO was used for visualization and analysis of the collected XrCT data. Segmentation of the data was performed to extract the material (SS316L) of the printed cylinder, using thresholding and

various tools offered through AVIZO. The total volume of the solid cylinders (without accounting for porosity) was calculated using AVIZO's internal tool. It is worth noting that due to the resolution used for the scanning (10 µm voxel size), only the total cylinder volume could accurately be determined. Ideally, a lower voxel resolution should be selected for the detection of both pores and micro pores present in the sample for a more accurate calculation. Figure **3-5** shows the post-sinter cylinders from the XrCT scans segmented and displayed in AVIZO. The high resolution achieved with the 10 µm voxel size can be seen from the figure, as well as some segmented porosity, shown in black. The porosity shown in the figure is only representative of a small fraction of the total porosity and is used as a visual to show more prominent pores.

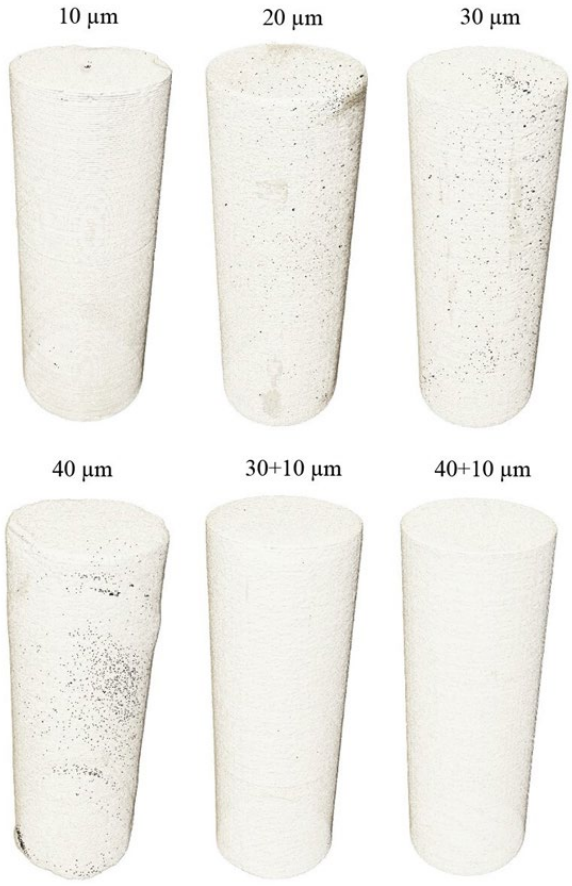

Figure **3-5**: AVIZO segmented cylinders from XrCT results.

3.3.2 Mechanical Testing

Printed bars (n=5 per group size) were used to measure the ultimate flexural strength via three-point bending test. This test was performed to obtain the maximum stress in the samples before breaking. An MTS Landmark 22 Kip servo hydraulic test frame was used for testing until complete rupture, following ASTM B528–16 standard at a 2.5 mm/min loading rate. In Eq. **(3- 2**) the formula used to calculate ultimate flexural strength (UFS) can be shown where F, L, w, t are the force required to rupture the specimen, the distance between the centers of the supporting rods, the width of the specimen, and the thickness of the specimen, respectively.

$$\sigma_{\max flex} = \frac{3FL}{2wt^2} \tag{3-2}$$

3.3.3 Statistical Analysis

Statistical analysis was performed on density values and UFS to determine any statistical differences between groups. Both sintered density (n=4) and UFS (n=5) results were compared based on powder size groups (6 groups). A Ryan-Joiner Test (similar to Shapiro-Wilk) was performed ($\alpha = 0.05$) in Minitab to verify if the data was normally distributed. If passed, the Bartlett's test for equal variance would be run. Both equal variance and normally distributed data are assumptions made by ANOVA and need to be tested. If both tests passed, a one-way ANOVA ($\alpha = 0.05$) would be performed, along with a Tukey Multiple Comparison test to compare group means.

However, if the normality test failed, a Kruskal-Wallis nonparametric test would be done in Python to evaluate the statistical difference in median values between groups. A Dunn's test, with a Bonferroni correction, would be used to indicate which groups are statistically different from

each other. The Bonferroni method would also be used to adjust the p-values, reducing family-wise error rate and the probability of Type I errors, which falsely reject the null hypothesis.

3.4 Results

3.4.1 Sintered Density

Sintered density results (n=4 cylinders measured with calipers) corresponding to each of the six particle size distribution groups are shown in Figure **3-6**. A visible trend within the unimodal groups is observed, showing a decrease in density as the particle sizes increase, up till 40 µm. The 40 µm density was found to be 5.11% and 6.77% larger than the 20 and 30 µm groups respectively. The 30+10 and 40+10 µm bimodal groups displayed a much higher density than any of the unimodal groups with average relative densities of 71.83% and 71.57%. Additionally, the 30+10 and 40+10 µm bimodal groups showed a 20.18% and 19.74% increase in sintered density when compared to the densest sample from the unimodal group, 10 µm.

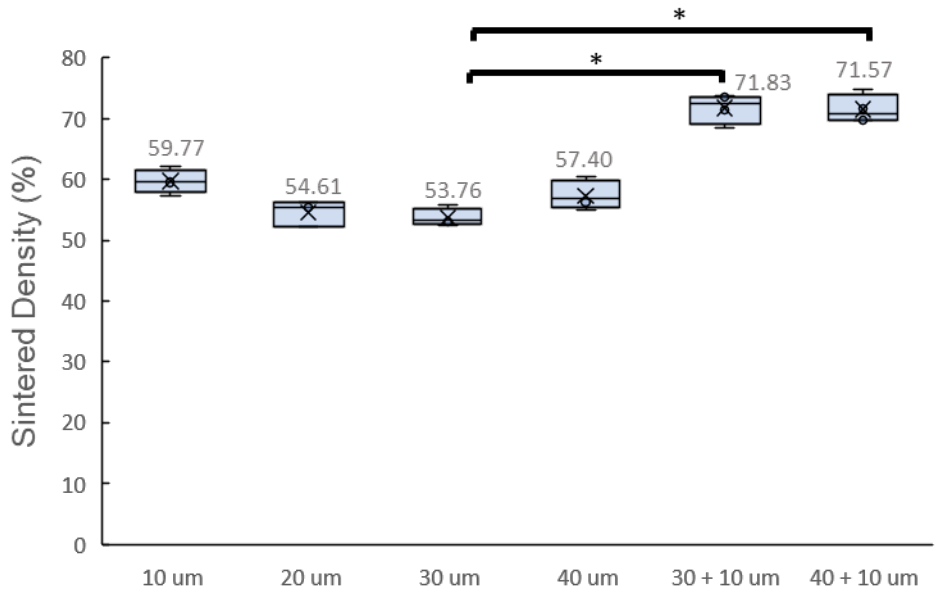

Figure **3-6**: Sintered density values measured using calipers for each particle size group, with mean values shown. *Bracket comparison denotes a p-value of 0.01-0.05.

The Ryan-Joiner test showed that the sintered density data presented was not normally distributed. Because of this, a Kruskal-Wallis ($\alpha = 0.05$) nonparametric test was performed, showing a p-value less than 0.05. This value indicated that due to the statistical difference between median values of each group, particle size distribution does have a statistical impact on the sintered density results obtained through this study. Upon the presented evaluation, a Dunn's test with Bonferroni correction found that the 30 µm group was the only group statistically lower than both bimodal groups as seen in Figure **3-6**. No other statistical difference was found between either the two bimodal groups, or any of the unimodal groups. The lack of statistical differences seen could be attributed to the low number of samples used, as this has a large impact on showing statistical significance.

Additional density measurements were calculated using the cylinder's volume extracted with XrCT data. Although a slight shift can be observed in the obtained XrCT densities when compared to the caliper averages presented above (a percent error of about 8.2%), the trends are consistent with each other. With XrCT data, the highest density was still achieved with both

bimodal groups at 74.82% and 76.99% followed by the unimodal 10 µm at 66.80%. In Figure **3-7,** a comparison between the results obtained using XrCT data, caliper measured data from the same sample number used in XrCT, and caliper average data (n=4 per group) is plotted.

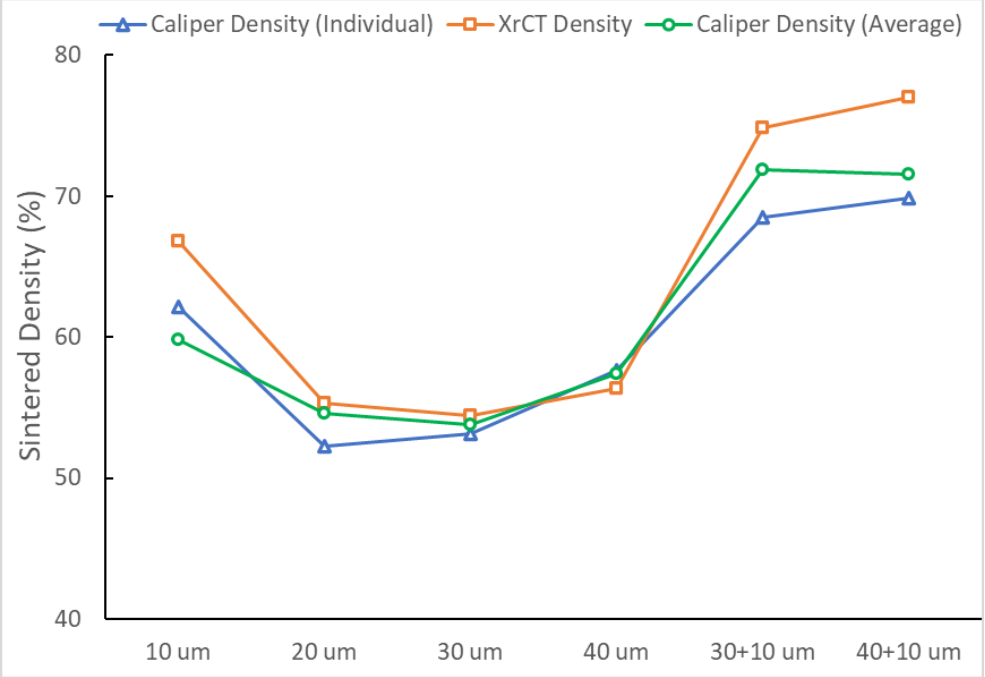

Figure **3-7**: Relationship and trend between all particle groups with respect to XrCT, caliper measured (individual), and caliper measured (average) density.

3.4.2 Three-Point Bending

Ultimate flexural strength results (n=5 bars) from each group, obtained from the three-point bending test, are shown in Figure **3-8**. A clear decreasing trend in UFS with an increase in particle size among the unimodal group can be observed, which agrees with the results found with the sintered density in Section 3.4.1. However, unlike the density trend reported previously, which saw a slight increase in 40 µm density compared to the 20 and 30 µm, with the presented results, there is a continuous decrease in UFS from 10 to 40 µm. Additionally, the 30+10 µm group was found to have on average lower UFS than the 40+10 µm, despite having an average higher density.

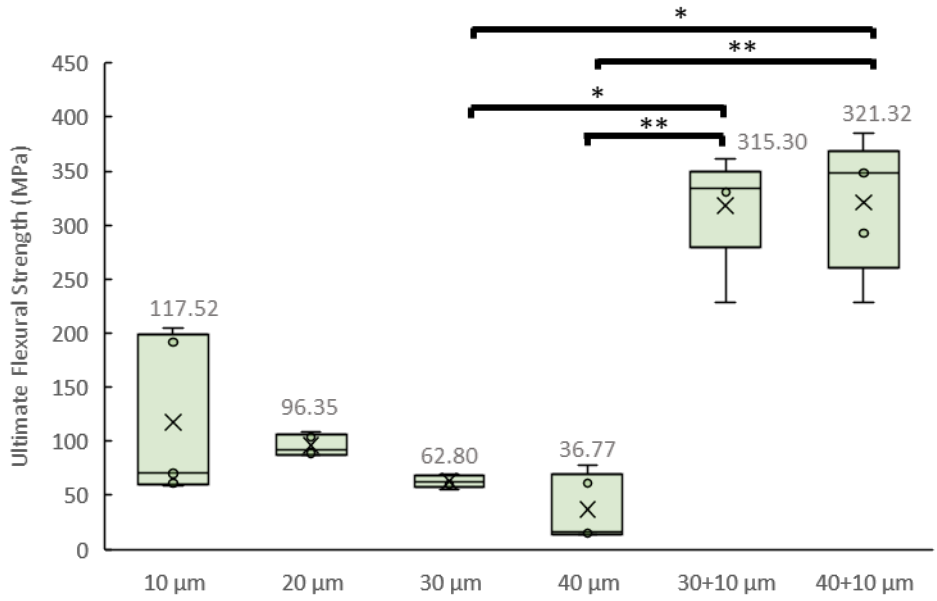

Figure **3-8**: Ultimate Flexural Strength (UFS) for each particle size group, with mean values shown. *Bracket comparison denotates a p-value of 0.01-0.05, and **Bracket comparison denotates a p-value < 0.01.

The Ryan-Joiner test also indicated that the Ultimate Flexural Strength (UFS) data was not normally distributed. The Kruskal-Wallis ($\alpha = 0.05$) nonparametric test was also performed. A p-value less than 0.05 was found, meaning there was a statistical difference in UFS between groups. A Dunn's test with Bonferroni correction was performed to determine which particle size groups had statistically different UFS. It was found that both bimodal groups were statistically higher than the 30 µm and 40 µm group from Figure **3-8**. Additionally, no statistical difference was found between either the two bimodal groups, or any of the unimodal groups.

Due to the size limitations of the tube furnaces used for sintering, only three bars were sintered at a time. Furnace variability was suspected to cause slight fluctuation in mechanical performance within particle groups, represented by the large relative standard deviation in the UFS data set collected, as seen in Table **3-4**. This may be an influencing factor on why statistical differences between some of the unimodal and bimodal groups were not observed, despite the

168.3% and 173.4% increase in UFS from the 10 µm to the 30+10 and 40+10 µm groups, respectively. Results gathered from samples that were sintered in the same batch were used to see the impact different sintered runs had on the UFS. It can be seen from Appendix Table 1, that when only looking at UFS values of a particle size groups sintered in the same batch, the RSD decreases. This indicates significant variations in strength between sintered groups. However, when both the truncated and full data sets are compared, Figure **3-8** and Appendix Figure **1**, a similar trend can be seen but different statistical significance.

Table **3-4**: Summary of results in mean and standard deviation for each of the particle groups.

Group	Sintered Density (%)			Ultimate Flexural Strength (MPa)		
	Mean	Std.	RSD	Mean	Std.	RSD
10 µm	59.77	1.98	3.31%	117.5	74.2	63.15%
20 µm	54.61	2.12	3.88%	96.35	9.81	10.18%
30 µm	53.76	1.43	2.66%	62.8	5.78	9.20%
40 µm	57.40	2.33	4.06%	36.8	30.8	83.70%
30+10 µm	71.83	2.47	3.44%	315.3	59.05	18.74%
40+10 µm	71.57	2.36	3.30%	321.3	61.8	19%

3.5 Discussions

Based on the results obtained in this study, it is suggested to use a bimodal distribution feedstock for the achievement of the highest density and preferred mechanical properties for SS316L. Results obtained with our work report a statistically significant increase in sintered density with the introduction of bimodal groups, compared to some of the unimodal distributions. This was expected, as it agrees with results found in other investigations that have used bimodal mixed powder [4], [19], [20]. The improvement in density, even after sintering conditions, could be attributed to the high packing behavior that bimodal particles offer. This behavior allows for more

contact area, which is beneficial for sintering and shrinkage reduction. To the best of the author's knowledge, no other study investigating the impact of bimodal against unimodal groups has achieved as large of a percent increase in sintered density as this investigation (20.18%).

The increase in density observed with our bimodal results aligns with Du et al.'s findings when studying silicon carbide. A 5% increase in bimodal green density was observed when compared with the unimodal distributions [26]. This increase in density was lower than the 20.18% obtained in our SS316L prints but the improvement in density is evident and is attributed to the bimodal distributions. Different powder morphologies, sizes, printing parameters, or material properties could have influenced the specific values obtained in their investigation when compared to this one. Additionally, Du et at. analyzed different coarse powder fractions (%) for bimodal mixing, finding the highest density values with 70-75% coarse particles in the mixture, which is comparable to the 73% used in this study.

The appropriate selection of a coarse to fine ratio has shown great impact in density results. The ratio used in this study has been found to achieve high packing density in other work. Bai et al. demonstrated in their work that although higher sintered density values were always achieved for metal materials utilizing bimodal distributions, different mixing ratios (1:3-1:6) would result in different values [19]. Depending on the duration at peak temperature, in some cases, 1:4 ratios displayed the highest density in copper when compared to other bimodal groups. In other cases, when the same peak temperature was sustained at a higher duration, the 1:5 ratio performed better. Although our results only investigated 1:3-1:4 ratios, the same peak temperature was sustained for the same amount of time. Although in some cases the 1:3 outperformed the 1:4 size mixing ratio, the lack of statistical difference between both groups highlights the adequacy of our coarse to fine particle selection.

In Section 3.4.2, Figure **3-6**, a clear trend within unimodal groups can be observed, highlighting the decrease in density with an increase in particle size. Similar results using SS316L

have been reported in the literature [27], [28], as well as in other metals [29] and ceramic materials [30]. Finer particles are known to enhance the sintering process because as they get closer, the initial bonding between them (also known as necking) initiates faster than with coarser particles. Additionally, the increase in surface energy and contact area associated with finer particles favors sinterability due to a higher particle bonding rate. It is worth highlighting that in Figure **3-6**, density decreases with an increasing particle size up until the 40 μm group, where a slight increase in density is observed. The authors attribute this possible outlier to something that may have occurred during the sintering stage. Furnace variability could be attributed to a combination of factors, including slight differences in sample positioning within the tube furnace and different gas flow rates. Temperature data was tracked and gathered during each of the sinter runs indicated that an identical heating profile was followed for all samples. It has been reported that the density SS316L metal injection molding parts were impacted by different gas atmospheres as well as other sintering factors [31]. Other papers have discussed the effects of sintering atmosphere on SS316L as well [32]. As tube furnaces only have a small hot zone, identical and precise placement of the samples in every run is difficult. Since the furnace used is available to other research groups, the standardization of the sintering process with respect to sample placement and gas flow rate monitoring is challenging. In order to alleviate this presented issue in the future, specific measurements of placement of the bars inside the alumina boat could be marked down as well as the precise placement of the boat inside the hot zone. Real time monitoring data should also be collected within runs to measure the gas flow rate.

As mentioned in section 3.4.2, a large standard deviation was observed with the full UFS data, as seen in Table **3-4**. This variation is believed to be caused by differences in sample position in the furnace, as explained above, or gas flow rate conditions within particle groups. Due to the lack of data of the specific gas flow rates used between sintering runs, the authors believe this might have had a slight impact on the variability of results. Argon is a heavy gas that is known to retain

heat. During the sintering stage of a binder jetting process, off gassing takes place as the binder is evaporated from the part (debinding). A higher gas flow rate might be beneficial for carrying these chemicals out of the furnace chamber and away from the part, as opposed to using a lower rate, which allows these gases to stay in the chamber interacting with the part for longer. As seen in Figure **3-9**, the differences between sintered runs of the same particle group have different colorations, indicating a slight difference in the gas atmosphere or flow rate. Additionally, as seen in Figure **3-9**a, gas flow lines are seen in only one of the samples, indicating the possible impact sample position might have on result variability. The truncated data contains samples only sintered at the same time, resulting in much lower standard deviations as seen in the Appendix Table **1**. This is believed to be further evidence that the higher density seen with the 40 μm cylinders might be caused by furnace variability. After performing data analysis on all sintered density values, the results showed no statistical difference between the 40 μm and any other unimodal groups. Regardless of the slight outlier, the results still find the bimodal groups to have a higher density when compared to the unimodal groups. Because of this, the authors confidently agree with the presented density results and conclusions.

Figure **3-9**: Different sinter runs (a and b) for the same particle size group. *Top right bar corresponds to a different group.

In general, a higher density results in higher mechanical strength because of the detrimental impact porosity has on mechanical performance. Evidence of this claim has been reported when working with SS316L where Jost et al. found that the ductility and strain at ultimate tensile strength for SS316L manufactured through PBF was negatively impacted by porosity [33]. Our results presented in Figure **3-8** agree with the claim that higher density (found in bimodal groups) corresponds to higher Ultimate Flexural Strength (UFS). As previously mentioned, the 40 µm group saw a slight deviation from the observed density trend within the unimodal group. Despite not having the lowest density, it was found that the 40 µm had the lowest UFS. Conclusions about this phenomenon rely on the possibility of surface porosity or open porosity present with that group. Because the sintered density was calculated using geometry measurements, the bulk volume (including open and closed pores) was used. Future investigations could rely on more advanced sintered density measurements such as the Archimedes method or He pycnometry for a more precise measurement.

The surface porosity might have resulted a high calculated density but lower strength. Reports of surface defects and roughness's impact on mechanical performance are highlighted in Masuo et al.'s work [34]. They found that surface roughness had a strong detrimental effect on fatigue strength of additively manufactured Ti-6Al-4V [34]. Overall, no statistical difference was found between unimodal groups. The high increase of bimodal UFS when compared to unimodal groups is still predominant at 315.30 and 321.32 MPa. Mechanical values presented with this work can be compared with a literature investigation where Shrestha et al. reported a maximum UFS of 90.10 MPa using binder jetting SS316L and the same sintering profile only with unimodal distributions. Due to the lack of UFS data for SS316L binder jetting in literature, Ultimate Tensile Strength (UTS) values can be used for comparison. In [2], Lecis et al. report SS316L binder jetting UTS values ranging from 534-540 MPa. Additionally, that same investigation reports even higher UTS values achieved from LPB and casting ranging from 620-695 MPa with the same material. It can be observed that the lower UFS values achieved in Section 3.4.2 could be attributed to the low densities achieved due to sinter profile used.

Finally, when looking at the obtained sintered density results regardless of particle size groups, the relative density (density calculated/theoretical density) was low (highest sintered density achieved was around 72%) compared to densities achieved by other studies. Based on literature reports, sintered density in binder jetting has in some cases reached around 95% depending on the specific material and the process parameters used. A reduction in density may be a consequence of insufficient sintering conditions, such as low sintered temperatures used (melting point of SS316L is around 1375 °C) and possible part expansion due to debinding caused by outgassing [19]. A higher sinter temperature should be considered to facilitate mass transport and increase the part density [35]. Additionally, as mentioned in Section 3.2.3, no work was done to obtain optimal printing process parameters. Based on other work, higher density values have been obtained by appropriately selecting specific process and thermal parameters that would enhance

the printing performance [2], [14] Future work should focus on finding different parameters and adjusting them for density increases, as well as investigating the impact of sintering profiles and their effect on bimodal distributions as they are directly affected by powder properties and packing state.

3.6 Conclusions

The goal of this study was to evaluate the impact bimodal distributions had on binder jetting SS316L parts. Six different particle distributions were compared, four unimodal (10 µm, 20 µm, 30 µm, 40 µm) and two bimodal (30+10 µm and 40+10 µm). An ExOne Innovent+ was used to print four cylinders and five bars per particle size group. The samples were cured and sintered; cylinders were used to calculate sintered density and bars were used for three-point bending. Caliper measures and XrCT data was collected from the cylinders calculate sintered density. Density and Ultimate Flexural Strength (found from three-point bending testing) were used to compare the impact of particle distribution. Based on the results, the main conclusions are:

- A bimodal powder distribution is preferred over unimodal distribution in binder jetting of SS316L, for higher density and preferred mechanical performance.
- Bimodal groups yielded higher sintered density values than any unimodal groups, achieving an increase of 20.18% and 19.74%.
- Bimodal groups showed a higher UFS than the unimodal groups. Both the 30+10 µm and 40+10 µm had a 168.3% and 173.4% increase, respectively, in UFS compared to the 10µm, which saw the highest UFS out of all unimodal groups.
- Bimodal groups saw no statistical difference between each other in density or UFS, according to the Dunn's test.

- It was found that for the unimodal groups presented, as particle size increases density decreases. The 10 μm had the highest density and was found to be higher than the lower achieved density from 30 μm, by 11.18%.
- UFS followed the same trend as density within the unimodal group; as particle size increases UFS decreases. The 10 μm group was found to have a higher UFS than the rest of the unimodal groups.
- Slight variation in the observed unimodal density trend is thought to may have been caused by furnace variability during sintering. This is also believed to may have caused large standard deviations in the full UFS data set.

Future work should be done to optimize the printing parameters of the bimodal groups to achieve the highest possible density and UFS. An investigation on alternate density measurement tools should also be considered. The effects of gas flow rate during sintering should be further investigated and studied, in addition to different sintering profiles and sample position. Finally, the effect of powder binder interaction in bimodal distributions as well as the specific tailoring of their sintering profiles for bimodal groups should be further looked into.

Acknowledgements

This work was funded by NSF CAREER CMMI #1944120. The authors acknowledge the support from The ExOne Company, The Pennsylvania State University, Tim Stecko, and Verder Scientific for their assistance.

References

[1] S. Mirzababaei and S. Pasebani, “A Review on Binder Jet Additive Manufacturing of 316L Stainless Steel,” J. Manuf. Mater. Process. 2019, Vol. 3, Page 82, vol. 3, no. 3, p. 82, Sep. 2019, doi: 10.3390/JMMP3030082.

[2] N. Lecis et al., “Effects of process parameters, debinding and sintering on the microstructure of 316L stainless steel produced by binder jetting,” Mater. Sci. Eng. A, vol. 828, p. 142108, Nov. 2021, doi: 10.1016/J.MSEA.2021.142108.

[3] M. Li, W. Du, A. Elwany, Z. Pei, and C. Ma, “Binder Jetting Additive Manufacturing of Metals: A Literature Review,” ASME 2019 14th Int. Manuf. Sci. Eng. Conf. MSEC 2019, vol. 1, Nov. 2019, doi: 10.1115/MSEC2019-2994.

[4] Y. Bai, G. Wagner, and C. B. Williams, “Effect of Bimodal Powder Mixture on Powder Packing Density and Sintered Density in Binder Jetting of Metals.”

[5] M. Li, W. Du, A. Elwany, Z. Pei, and C. Ma, “Metal binder jetting additive manufacturing: A literature review,” J. Manuf. Sci. Eng. Trans. ASME, vol. 142, no. 9, Sep. 2020, doi: 10.1115/1.4047430/1084395.

[6] I. Gibson, D. Rosen, B. Stucker, and M. Khorasani, “Binder Jetting,” Addit. Manuf. Technol., pp. 237–252, 2021, doi: 10.1007/978-3-030-56127-7_8.

[7] M. Ziaee, E. M. Tridas, and N. B. Crane, “Binder-Jet Printing of Fine Stainless Steel Powder with Varied Final Density,” doi: 10.1007/s11837-016-2177-6.

[8] G. K. Meenashisundaram, Z. Xu, M. L. S. Nai, S. Lu, J. S. Ten, and J. Wei, “Binder Jetting Additive Manufacturing of High Porosity 316L Stainless Steel Metal Foams,” Mater. 2020, Vol. 13, Page 3744, vol. 13, no. 17, p. 3744, Aug. 2020, doi: 10.3390/MA13173744.

[9] J. Vogt et al., “Improved green and sintered density of alumina parts fabricated by binder jetting and subsequent slurry infiltration,” Prog. Addit. Manuf. 2021, pp. 1–11, Dec. 2021, doi: 10.1007/S40964-021-00222-1.

[10] Q. Porter, Z. Pei, and C. Ma, “Binder Jetting and Infiltration of Metal Matrix Nanocomposites,” J. Manuf. Sci. Eng., pp. 1–8, Dec. 2021, doi: 10.1115/1.4053156.

[11] A. Yegyan Kumar, Y. Bai, A. Eklund, and C. B. Williams, “The effects of Hot Isostatic Pressing on parts fabricated by binder jetting additive manufacturing,” Addit. Manuf., vol. 24, pp. 115–124, Dec. 2018, doi: 10.1016/J.ADDMA.2018.09.021.

[12] A. Kumar, Y. Bai, A. Eklund, and C. B. Williams, “Effects of Hot Isostatic Pressing on Copper Parts Fabricated via Binder Jetting,” Procedia Manuf., vol. 10, pp. 935–944, Jan. 2017, doi: 10.1016/J.PROMFG.2017.07.084.

[13] T. Dahmen et al., “Densification, microstructure, and mechanical properties of heat-treated MAR-M247 fabricated by Binder Jetting,” Addit. Manuf., vol. 39, p. 101912, Mar. 2021, doi: 10.1016/J.ADDMA.2021.101912.

[14] S. Shrestha and G. Manogharan, “Optimization of Binder Jetting Using Taguchi Method,” JOM, vol. 69, no. 3, pp. 491–497, Mar. 2017, doi: 10.1007/s11837-016-2231-4.

[15] “Effect of Bimodal Powder Mixture on Powder Packing Density and Sintered Density in Binder Jetting of Metals .” http://utw10945.utweb.utexas.edu/sites/default/files/2015/2015-62-Bai.pdf (accessed Dec. 20, 2021).

[16] W. Du, M. Singh, and D. Singh, “Binder jetting additive manufacturing of silicon carbide ceramics: Development of bimodal powder feedstocks by modeling and experimental methods,” Ceram. Int., vol. 46, no. 12, pp. 19701–19707, Aug. 2020, doi: 10.1016/j.ceramint.2020.04.098.

[17] W. Du, X. Ren, Y. Chen, C. Ma, M. Radovic, and Z. Pei, “Model Guided Mixing of Ceramic Powders With Graded Particle Sizes in Binder Jetting Additive Manufacturing,” ASME

2018 13th Int. Manuf. Sci. Eng. Conf. MSEC 2018, vol. 1, Sep. 2018, doi: 10.1115/MSEC2018-6651.

[18] W. Du, J. Roa, J. Hong, Y. Liu, Z. Pei, and C. Ma, "Binder Jetting Additive Manufacturing: Effect of Particle Size Distribution on Density," J. Manuf. Sci. Eng., vol. 143, no. 9, Sep. 2021, doi: 10.1115/1.4050306.

[19] Y. Bai, G. Wagner, and C. B. Williams, "Effect of particle size distribution on powder packing and sintering in binder jetting additive manufacturing of metals," J. Manuf. Sci. Eng. Trans. ASME, vol. 139, no. 8, Aug. 2017, doi: 10.1115/1.4036640.

[20] R. Batmaz et al., "An Investigation into Sinterability Improvements of 316L Binder Jet Printed Parts," Metall. Mater. Trans. A 2021, pp. 1–12, Jan. 2022, doi: 10.1007/S11661-021-06564-3.

[21] A. Paula Clares and G. Manogharan, "DISCRETE-ELEMENT SIMULATION OF POWDER SPREADING PROCESS IN BINDER JETTING, AND THE EFFECTS OF POWDER SIZE," 2021, Accessed: Jan. 23, 2022. [Online]. Available: http://asmedigitalcollection.asme.org/MSEC/proceedings-pdf/MSEC2021/85062/V001T01A009/6736395/v001t01a009-msec2021-63351.pdf.

[22] "ISO - ISO/ASTM 52900:2015 - Additive manufacturing — General principles — Terminology." https://www.iso.org/standard/69669.html (accessed Nov. 17, 2020).

[23] H. Chen and Y. F. Zhao, "Process parameters optimization for improving surface quality and manufacturing accuracy of binder jetting additive manufacturing process," Rapid Prototyp. J., vol. 22, no. 3, pp. 527–538, 2016, doi: 10.1108/RPJ-11-2014-0149/FULL/PDF.

[24] B. Utela, D. Storti, R. Anderson, and M. Ganter, "A review of process development steps for new material systems in three dimensional printing (3DP)," J. Manuf. Process., vol. 10, no. 2, pp. 96–104, Jul. 2008, doi: 10.1016/J.JMAPRO.2009.03.002.

[25] A. Mostafaei et al., “Binder jet 3D printing – Process parameters, materials, properties, and challenges,” Progress in Materials Science. Elsevier Ltd, p. 100707, Jun. 15, 2020, doi: 10.1016/j.pmatsci.2020.100707.

[26] W. Du, M. Singh, and D. Singh, “Binder jetting additive manufacturing of silicon carbide ceramics: Development of bimodal powder feedstocks by modeling and experimental methods,” Ceram. Int., vol. 46, no. 12, pp. 19701–19707, Aug. 2020, doi: 10.1016/J.CERAMINT.2020.04.098.

[27] H. Miyanaji, N. Momenzadeh, and L. Yang, “Effect of powder characteristics on parts fabricated via binder jetting process,” Rapid Prototyp. J., vol. 25, no. 2, pp. 332–342, Feb. 2019, doi: 10.1108/RPJ-03-2018-0069/FULL/PDF.

[28] B. Verlee, T. Dormal, and J. Lecomte-Beckers, “Density and porosity control of sintered 316L stainless steel parts produced by additive manufacturing,” http://dx.doi.org/10.1179/0032589912Z.00000000082, vol. 55, no. 4, pp. 260–267, Sep. 2013, doi: 10.1179/0032589912Z.00000000082.

[29] Y. Bai and C. B. Williams, “An exploration of binder jetting of copper,” Rapid Prototyp. J., vol. 21, no. 2, pp. 177–185, Mar. 2015, doi: 10.1108/RPJ-12-2014-0180/FULL/PDF.

[30] M. Moghadasi, W. Du, M. Li, Z. Pei, and C. Ma, “Ceramic binder jetting additive manufacturing: Effects of particle size on feedstock powder and final part properties,” Ceram. Int., vol. 46, no. 10, pp. 16966–16972, Jul. 2020, doi: 10.1016/J.CERAMINT.2020.03.280.

[31] C. H. Ji, N. H. Loh, K. A. Khor, and S. B. Tor, “Sintering study of 316L stainless steel metal injection molding parts using Taguchi method: final density,” Mater. Sci. Eng. A, vol. 311, no. 1–2, pp. 74–82, Jul. 2001, doi: 10.1016/S0921-5093(01)00942-X.

[32] T. M. Sridhar, U. Kamachi Mudali, and M. Subbaiyan, “Sintering atmosphere and temperature effects on hydroxyapatite coated type 316L stainless steel,” Corros. Sci., vol. 45, no. 10, pp. 2337–2359, Oct. 2003, doi: 10.1016/S0010-938X(03)00063-5.

[33] E. W. Jost, J. C. Miers, A. Robbins, D. G. Moore, and C. Saldana, “Effects of spatial energy distribution-induced porosity on mechanical properties of laser powder bed fusion 316L stainless steel,” Addit. Manuf., vol. 39, p. 101875, Mar. 2021, doi: 10.1016/J.ADDMA.2021.101875.

[34] H. Masuo et al., “Effects of Defects, Surface Roughness and HIP on Fatigue Strength of Ti-6Al-4V manufactured by Additive Manufacturing,” Procedia Struct. Integr., vol. 7, pp. 19–26, Jan. 2017, doi: 10.1016/J.PROSTR.2017.11.055.

[35] W. Du, X. Ren, Z. Pei, and C. Ma, “Ceramic Binder Jetting Additive Manufacturing: A Literature Review on Density,” J. Manuf. Sci. Eng., vol. 142, no. 4, Apr. 2020, doi: 10.1115/1.4046248.

Chapter 3 Appendix

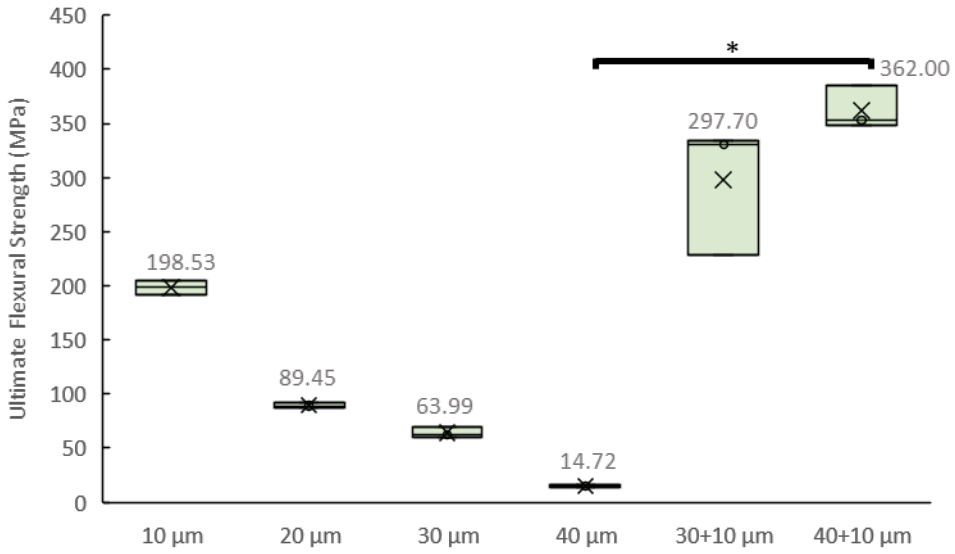

Figure **1**: Truncated Data-Ultimate Flexural Strength (UFS) for each particle size group, with mean values shown. *Bracket comparison denotates a p-value of 0.01-0.05.

Table **1**: Truncated Data-Summary results of the full data set of three-point bending test.

Group	Ultimate Flexural Strength (MPa)		
	Mean	Std.	RSD
10 µm	198.53	9.5	4.78%
20 µm	89.45	2.88	3.21%
30 µm	63.99	4.78	7.47%
40 µm	14.72	1.323	8.99%
30+10 µn	297.70	59.9	20.10%
40+10 µn	362.00	20.1	5.55%

Chapter 4

Conclusions and Future Work

Binder jetting is one of the seven additive manufacturing technologies that has quickly gained attention in industry and academia due to the multiple unique advantages offered. The wide range of material selection, absence of rapid-melting solidification defects, high production rates, and large build volumes have made this process a feasible alternative to traditional methods and other AM technologies. Despite these promising advancements, one of the biggest challenges binder jetting still faces is achieving high density green bodies. Typically, extensive post-processing steps, such as sintering and material infiltration, are necessary to fully densify and obtain desired part characteristics. Material-related parameters such as powder size distribution have been studied as alternative means to improve density and have demonstrated a large impact in packing density and flowability. Although previous research has highlighted the positive impact of bimodal particle mixtures in binder jetting, findings are focused on specific materials, or limited to particular evaluating conditions. The work presented in this thesis better connects novel computational models with experimental validation to gain a greater understanding of the fundamental impact bimodal mixtures have on packing density, sintered density, and mechanical properties. Chapter 1 highlights the advantages and limitations of binder jetting compared to other AM techniques and the importance of material related parameters such as particle size distribution.

Chapter 2 introduces a computational model using the discrete-element-method (DEM) to study powder spreading within the binder jetting process. This chapter presents powder spreading simulations using three different powder size groups to investigate the fundamental impact powder size distribution has on packing density (using bulk volume and mass), flowability (measured with repose angle), and porosity. This work used two unimodal groups (one fine and one coarse) and one bimodal. It was found that the coarse unimodal powder size resulted in a higher flowability

with a 62% decrease in repose angle when compared to the fine unimodal powder size. Additionally, the results collected demonstrated that powder size distribution had a statistically significant influence on packing density. The bimodal size distribution yielded the highest density with an 8% increase in packing density and a 12% porosity reduction compared to the other groups.

In Chapter 2, simulation results highlighted the improvement in density by introducing bimodal mixtures. In Chapter 3, the experimental validation of this claim was investigated, as well as the evaluation of bimodal mixtures' impact on sintered density mechanical performance. Six different particle size distributions were compared (four unimodal and two bimodal groups). The printed samples were cured and sintered, and density results were measured using digital calipers and X-ray computed tomography (XrCT). It was found that a higher XrCT voxel resolution was required for accurate pore characterization and quantification. Due to the presence of small pores and 10 μm voxel resolution, greyscale noise made it difficult to differentiate between voids and the solid cylinder. Three-point bending tests were completed, measuring ultimate flexural strength (UFS) of the different particle groups. Overall, results showed a clear improvement with bimodal distributions. Statistical differences were observed between unimodal and bimodal groups, showing an increase in sintered density by 20.18% and 19.74% with the introduction of both bimodal size groups. Additionally, a 168.3% and 173.4% increase in UFS was observed when comparing both bimodal size groups to the highest performing unimodal group.

This thesis highlights the significant role particle size distribution plays during the binder jetting process. In particular, the results obtained serve to advance the industry of binder jetting to produce high-density parts, comparable to those manufactured using traditional methods. Results from this work confirm the central hypothesis proposed in Chapter 1 that bimodal particle size distributions can increase density and improve the mechanical performance of binder jetting parts. Although both computational and experimental results statistically show the positive impact of

bimodal mixtures, additional research avenues should be pursued to advance the efforts and findings of this thesis.

Based on the results presented in this thesis, future efforts in binder jetting should address the following areas. In Chapter 2, although the DEM has successfully proved to be an effective method for powder spreading simulation, there is still a gap in understanding the binder-powder interactions. Simulation work could be extended to account for binder droplet generation. This additional step included in the simulation would allow the evaluation of binder permeation and wettability in bimodal mixtures and to understand the impact on green strength. Additionally, due to the key impact the sintering stage has on a binder jetting process, computational work could be extended to simulate the sintering process using bimodal size distributions.

In Chapter 3, despite achieving the highest densities and UFS with bimodal distributions, the overall relative density of about 72%, was low. Future efforts should be directed towards parameter optimization with investigations tailored specifically to bimodal size distributions. Due to the limitations presented with the sintered density measurements, additional methods such as Archimedes could be employed in the future. In that same chapter, slight variations in the data, believed to be introduced in the sintering stage, are discussed. The overall trends and statistical significance between bimodal and unimodal groups did not change, but some outliers were reported. For example, it was observed that as particle size increased, sintered density decreased, until it reached 40 μm. A slight increase in density was observed with the 40 μm particles, deviating slightly from the overall trend. It was speculated that furnace variability may have caused data fluctuations; UFS data showed small standard deviation between intergroup samples sintered at the same time but large differences between samples sintered at different times. The effect of gas flow rate on the binder jetting sintering process should be examined in future work, as well as the different positioning of the samples throughout the hot zone of the furnace. Additionally, the evaluation of a specific sinter temperature profile for bimodal mixtures should be explored.

Addressing the poorly understood research areas outlined here will enable achieving higher densities in binder jetting though bimodal powder distributions and give more consistent post-sintered results.